https://doi.org/10.5194/egusphere-2023-2
Preprint. Discussion started: 9 February 2023

Remotely Sensed and Surface Measurement Derived Mass-Conserving Inversion of Daily High-Resolution NO_x Emissions and Inferred Combustion Technologies in Energy Rich Northern China

Xiaolu Li[1,2], Jason Blake Cohen[2]*, Kai Qin[2], Hong Geng[1], Liling Wu[4], Xiaohui Wu[3], Chengli Yang[3], Rui Zhang[5], Liqin Zhang[6]

[1]Institute of Environmental Science, Shanxi University, Taiyuan, 030006, China
[2]School of Environment and Spatial Informatics, China University of Mining and Technology, Xuzhou, 221116, China
[3]Shanxi Dadi Eco-environmental Technology Research Institute Co., Taiyuan, 030000, China
[4]School of Environment, Tsinghua University, Beijing, 10084, China
[5]Shanxi Institute of Eco-environmental Planning and Technology, Taiyuan, 030002, China
[6]Shanxi Institute of Eco-environmental Monitoring and Emergency Response Center, Taiyuan, 030027, China

Correspondence to: Jason Blake Cohen (jasonbc@alum.mit.edu)

Abstract. This work presents a new model free inversion estimation framework using daily TROPOMI NO_2 columns and observed fluxes from the continuous emissions monitoring systems (CEMS) to quantify three years of daily-scale emissions of NO_x at 0.05°×0.05° over Shanxi Province, a major world-wide energy producing and consuming region. The NOx emissions, day-to-day variability, and uncertainty on a climatological basis are computed to be 1.83, 1.01, and 1.06 Tg per year respectively. The highest emissions are concentrated in the lower Fen River valley, which accounts for 25% of the area, 52% of the NO_x emissions, and 72% of CEMS sources. Two major forcing factors (10^{th} to 90^{th} percentile) are horizontal transport distance per day (66-666 km) and lifetime of NO_x (6.7-18.4 h). Both of these values are consistent with NO_x emissions to both the surface layer and the free troposphere. The third forcing factor, the ratio of NO_x/NO_2, on a pixel-by-pixel basis is demonstrated to have a significant correlation with the combustion temperature and energy efficiency of large energy consuming sources. Specifically, thermal power plants, cement, and iron and steel companies have a relatively high NO_x/NO_2 ratio, while coking, industrial boilers, and aluminium oxide show relatively low ratio. Variance maximization is applied to daily TROPOMI NO_2 columns identifies three significant modes, and successfully attributes them both spatially and temporally to (a) this work's computed emissions, (b) remotely sensed TROPOMI UVAI, and (c) computed transport based on TROPOMI NO_2.

https://doi.org/10.5194/egusphere-2023-2
Preprint. Discussion started: 9 February 2023

Graphical abstract.

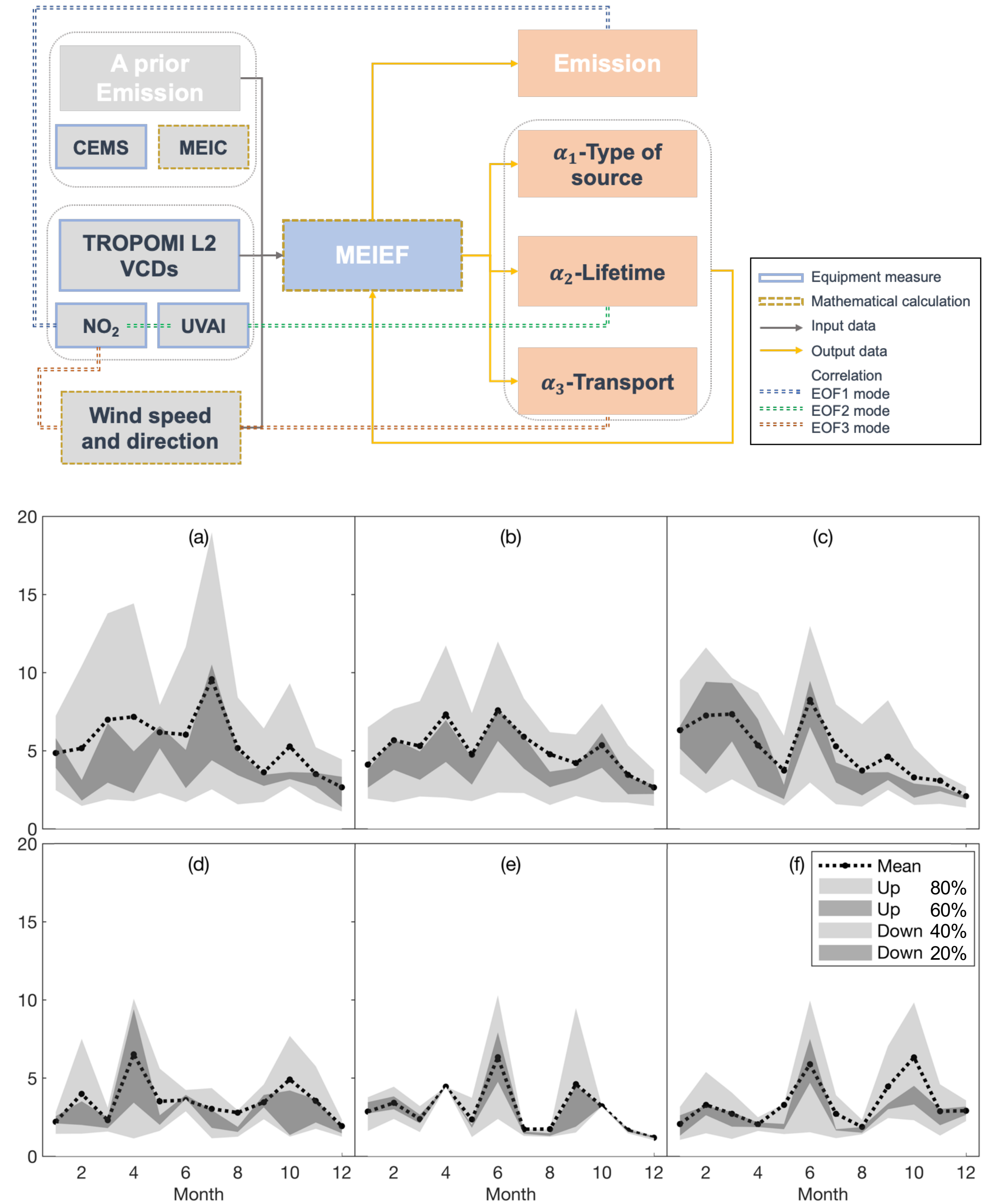

https://doi.org/10.5194/egusphere-2023-2
Preprint. Discussion started: 9 February 2023

1 Introduction

Economic growth has always been accompanied by air pollution, with serious consequences associated with non-green economic growth are more serious. To alleviate severe air quality problems, the Chinese government has been implementing new air pollution controls, with the aim of producing higher-quality development. Two recent examples are the Air Pollution Prevention and Control Action Plan from 2013 to 2017 and the Three-Year Action Plan for Winning the Battle in Defense of Blue Sky from 2018 to 2020 (Geng et al., 2019; Jiang et al., 2021), which have led to a significant reduction in annual average concentration of particulate matter (PM), sulfur dioxide (SO_2) and carbon monoxide (CO) in Shanxi Province. Shanxi is selected for this study, with geographical location and topography showed in Fig. 1, as it is a highly energy rich location that produces more than 25% of all of China's coal, as well as having substantial industry that consumes a significant amount of coal for both local energy production and export, steel, cement, coke, and aluminum production, among other economic activities (Li et al., 2022). However, there have also been minor increases in the observed annual average concentration of both ozone (O_3) and nitrogen dioxide (NO_2) in Shanxi between 2015 and 2020 (2015, 2020). Furthermore, due to its relatively dry climate, high elevation, and mountainous geography, it has complex underlying natural factors also impacting its atmospheric environment.

The sum of NO_2 and Nitrogen Monoxide (NO) is frequently grouped as nitrogen oxides (herein termed NO_x), which is an important trace gas impacting of the earth's atmosphere because it is a strong marker of anthropogenic combustion-related pollution, a precursor to ozone (Jacob et al., 1993), secondary aerosol (Beirle et al., 2011) and acid rain (Singh and Agrawal, 2007). In order to gain a better understanding of NO_x and its impacts, precise and quantitative emissions inventories are crucial information for policy makers, air quality modelers, climate change modelers, and those who conduct pollution weather response interactions, among others (Hoesly et al., 2018; Crippa et al., 2018; Li et al., 2017a). However, it is challenging to quantify emissions in rapidly developing and changing areas accurately as there are a variety of contributing sources, a complex underlying mixture of combustion technologies, industrial restructuring, changing population dynamics, and ongoing atmospheric environmental management, all of which may lead to substantial changes in pollution sources.

Presently, most emission inventories are compiled from statistics on emitting activities and associated typical emission factors, herein called "bottom-up" approaches (Ohara et al., 2007; Zheng et al., 2018; Li et al., 2017b). Bottom-up methods provide emissions data at finer scales. However, higher resolution emission inventories using bottom-up methods require rich, detailed, and extremely precise records of energy use, facility locations, and other socioeconomic datasets from multiple regional and temporal scales (Cai et al., 2018), which frequently have a considerable amount of uncertainty (Bond et al., 2007). With the ever-increasing tightening of environmental management, emission factors have changed significantly and will continue to do so in the future. On-site surveys for bottom-up methods are time consuming and resource demanding. When performing emission factor determination in laboratory, it is important to note that differences between small field studies and controlled laboratory combustion experiments and real-world examples also are quite significant, with super-emitters known to create large differences when using insufficiently large datasets (Zavala et al., 2006) and missing large sources leading to significant

https://doi.org/10.5194/egusphere-2023-2
Preprint. Discussion started: 9 February 2023

error (Wang et al., 2021). Due to the low temporal resolution and time-lag associated with many of these datasets being available, bottom-up inventories are not easy to keep up with rapid changes in industrial, economic, and pandemic, and therefore are not very good at tracking atmospheric emissions under actual existing environmental conditions, limiting their use (Mijling and Van Der A, 2012).

To overcome the disadvantages identified above, while simultaneously improving the spatial and temporal resolution of emission inventories, attempts at top-down emissions inventories using remote sensed dataset have been made by the community. Some of these attempts have focused on applications to long-lived gasses (CH_4, CFCs, and N_2O), since their chemical decay is very slow compared with their transport processes, allowing a simpler set of approximations to perform the inversion (Chen and Prinn, 2006; Tu et al., 2022b; Liu et al., 2021). Satellite observations have also been widely used to quantify short-lived species such as NO_x emissions (Martin, 2003; Beirle et al., 2019; Goldberg et al., 2019; Qu et al., 2019) by providing up-to-date and continuous time series of NO_2 columns in different region. Gaussian plumes have been used for a long time (Green et al., 1980), with more advanced but similar approximations including the exponentially modified gaussian model to quantify the NO_x emissions of isolated megacity sources (Beirle et al., 2011) and the probabilistic collocation method to train the emissions flux enhancement of megacities as a function of their size and shape (Cohen and Prinn, 2011). Some methods used a partial estimation of the mass balance approaches, including Kong et al. (Kong et al., 2019) and Beirle et al. (Beirle et al., 2019), which have assumed that some of the mass-based-terms are negligible, or some of the factors underlying the terms are very narrowly constrained. Another category based on atmospheric chemical transport or climate models and data assimilation, such as 3D-Var, 4D-Var, and Kalman filters work very well but are susceptible to underlying model and scientific uncertainty, as well as being extremely costly to run (Cohen and Wang, 2014; Zhang et al., 2021). The selection of a priori inventories is crucial when using the methods above, since it has been demonstrated that missing sources can frequently not be compensated for by increasing other sources if the spatial and temporal distributions are not matched correctly (Cohen, 2014). At the present time, some of the most accepted emissions inventories include the Multi-resolution Emission Inventory for China (MEIC) and the Emission Database for Global Atmospheric Research (EDGAR) (Crippa et al., 2018). In recent years, continuous emissions monitoring systems (CEMS) have been introduced in China, the USA, and other locations, as a means to detect in an integrated manner at the emissions effluent source, on an hourly and/or daily time scale, and contains well-known aspects of quality control and assurance. This platform provides reliable technical information to fundamentally quantify local emissions on a stack-by-stack basis, in order to improve both the temporal resolution and magnitude of emission inventories (Tang et al., 2019; Gu et al., 2022; Chen et al., 2019; Lange et al., 2022).

This study takes advantage of the respective strengths of top-down and bottom-up emissions estimation by applying a new, fast, first-order approximation of physical, chemical, and thermodynamics controlling the distribution of NO_x in situ, and constrains these approximations using daily measurements of remotely sensed NO_2 from the Tropospheric Monitoring Instrument (TROPOMI) using a mass conserving inversion to estimate the daily NO_x emissions on a mesoscale grid at (0.05°×0.05°) from January 2019 through December 2021. This net combination of factors does not rely on complex models,

https://doi.org/10.5194/egusphere-2023-2
Preprint. Discussion started: 9 February 2023

and allows a flexible approximation which can be modified by the user for various applications. The a prior emission in this work have used both daily-resolution CEMS and MEIC over Shanxi province. This unique perspective is capable of inverting emissions as a function of their month-to-month constrained driving forces, under different but realistic environmental conditions. The fact that three years of driving data have been used over different months of the year, over multi-year changes in the environment, under high UV and low UV conditions, under complex meteorological domains, over sources which are both thermodynamically stable as well as unstable, and even through COVID-19, permits this study to fully explore the full range of variations observed. Additionally, this approach allows a robust error quantification, and compares well with the measured spatial and temporal variation in the underlying remotely sensed NO_2 columns.

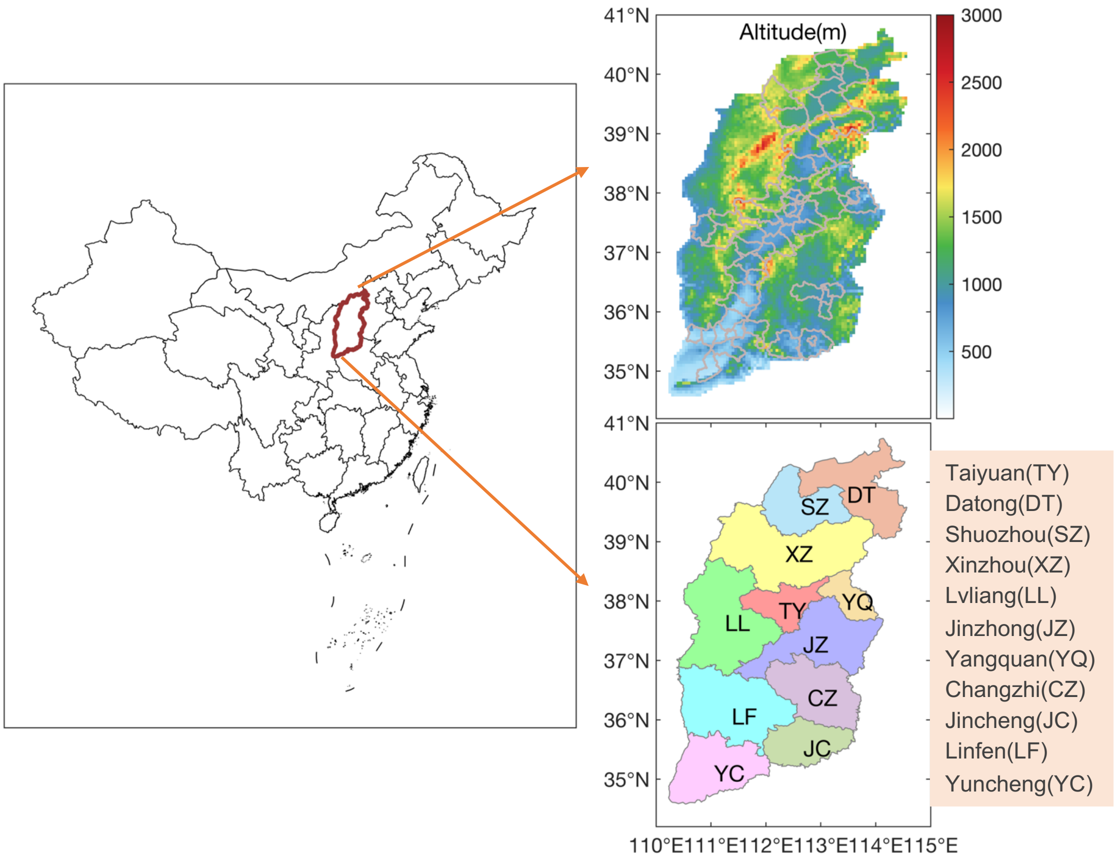

Figure 1: Location, topography and administrative division of Shanxi Province.

2 Materials and Methods

2.1 Tropospheric Vertical Column Measurements from TROPOMI

TROPOMI measures reflected solar radiation in the UV, visible, and Near IR bands following a sun-synchronous, low-earth orbit with an equator overpass time of approximately 13:30 LT, allowing daily-scale measurements across the globe (Veefkind

https://doi.org/10.5194/egusphere-2023-2
Preprint. Discussion started: 9 February 2023

et al., 2012; Goldberg et al., 2019; Tu et al., 2022a). Starting from August 2019, the spatial resolution of TROPOMI has been refined to 5.5 km×3.5 km (Lange et al., 2022). This study uses two distinct products measured by TROPOMI over different radiative bands, but at the same place and time: NO_2 and UVAI.

Daily level-2 version 2.3.1 tropospheric NO_2 columns and version 2.2.0 UVAI over Shanxi Province has been introduced. All available days and swaths corresponding to the time period from 1 January 2019 through 31 December 2021 are analyzed (https://disc.gsfc.nasa.gov/datasets). Overlapping NO_2 and UVAI column pixels in each swath are resampled to a common latitude-longitude grid at 0.05 °×0.05 ° using weighted polygons (http://stcorp.github.io/harp/doc/html/index.html). Before use, it is required that all TROPOMI data is quality assured, specifically insisting that each pixel has a "qa_value" greater than 0.75, that the "cloud radiance fraction" is smaller than 0.5, and that scenes covered by snow/ice, errors and similar problematic retrievals are removed (Henk Eskes, 2021). Furthermore, in the case of NO_2, an additional filter is applied to avoid issues where the signal is possibly smaller than the uncertainty about 30% to 50% (Qin et al., 2022; Steven Compernolle, 2018), leading to all grids with a column loading smaller than 1.4×10^{15} molec cm^{-2} being discarded. This combination of assumptions ensures that the data used should be of the highest possible precision based on the current available technology.

The average loading, daily variation, and number of days without TROPOMI NO_2 columns from 2019 through 2021are shown in Fig. 2. The number of invalid days varies pixel-by-pixel from 357 to 742 (521 on average), with higher altitude and mountainous areas tending to be more. The TROPOMI NO_2 columns used in this study can portray the spatial and temporal distribution of sources in a high amount of detail, including being able to effectively identify spatial hotspots (Griffin et al., 2019). The higher values on the maps are consistent with known urban and industrial regions, such as Taiyuan Basin, Xinding Basin, Linfen Basin, and Yangquan City. Areas with a high variation and relatively low mean value are observed in regions where new economic development zones have been recently created or are in the process of being actively developed, including urban areas of Datong and Xinzhou. Areas with a relatively high variation and high mean value are indicative of high urbanization and developed industrial areas, corresponding with the Taiyuan Basin, and southern Yangquan. Areas with a high average value and a low variation correspond with areas which have a fewer number of temporally consistent emissions sources, as is observed in parts of the Linfen Basin, central Changzhi, Lvliang and Jincheng, and industrial parks in Jiexiu district of Jinzhong.

https://doi.org/10.5194/egusphere-2023-2
Preprint. Discussion started: 9 February 2023

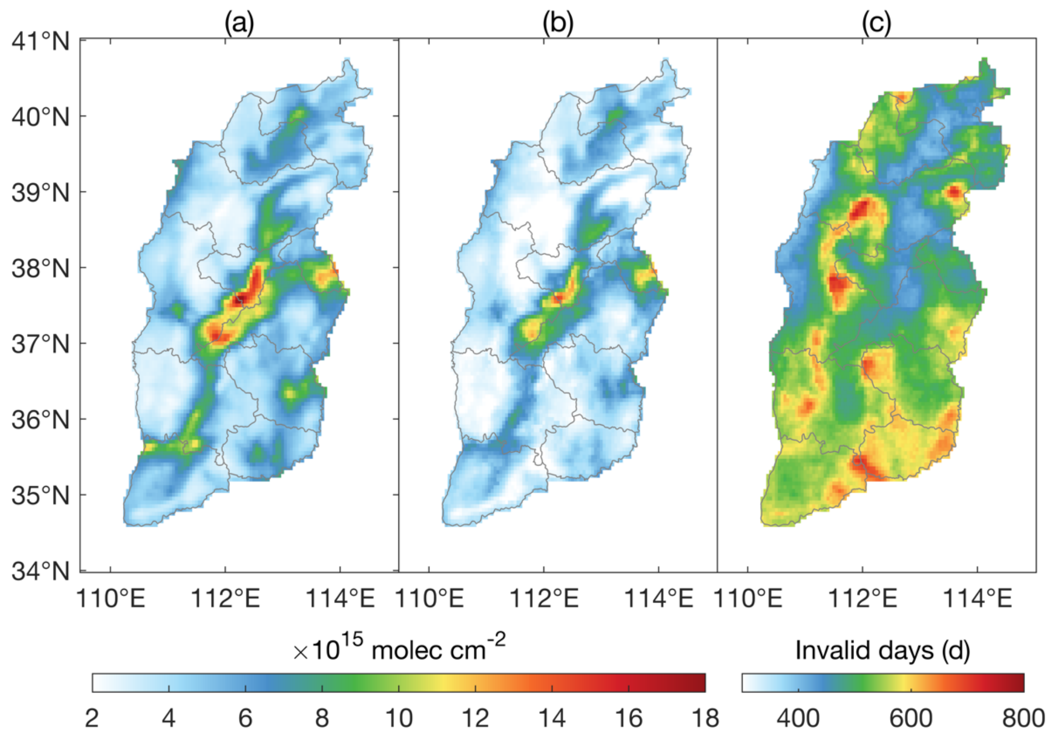

Figure 2: TROPOMI daily NO_2 column loadings from 2019 through 2021: (a) mean value (unit: molec cm^{-2}), (b) day by day standard deviation (unit: molec cm^{-2}), and (c) the number of invalid days (unit: d).

2.2 A Prior Emissions inventories

2.2.1 CEMS

CEMS was introduced by the Ministry of Environmental Protection of China in 2007 to monitor and manage the emissions of certain (mainly high-emitting) plants (Schreifels et al., 2012; Karplus et al., 2018). CEMS makes actual stack flue gas measurements of the concentration of PM, SO_2 and NO_x as discharged from coal power plants, steel and iron plants, aluminum smelters, coke plants, coal-fired boilers and others, all in real-time (Tang et al., 2020; Zhang and Schreifels, 2011). Statistics of the emissions sites monitored in Shanxi are given in Table1. There are two different technologies for NO_x concentration measuring. One converts NO_2 to NO and measures the total NO concentration, the other measures NO_2 and NO separately. Both of the measured results have been converted to NO_2 mass concentration.

In this work, all available CEMS monitors of daily-scale emissions from 2019 to 2021 were obtained from the Department of Ecology and Environment of Shanxi Province, with the government making great effort to regulate the CEMS network and to ensure the reliability of CEMS data (Tang et al., 2020). Preprocessing includes using google earth to correct the location of the factories, conducting quality control on measured concentrations according to the CEMS technical requirements, including eliminating negative values, outlier values, and null values. The overall percentage of abnormal values is found to account for

https://doi.org/10.5194/egusphere-2023-2
Preprint. Discussion started: 9 February 2023

0.63%, 1.18%, and 1.55% of the raw data respectively for 2019, 2020 and 2021. The formula used to calculate NO_x emissions is given in Eq. (1):

$$E_d = \overline{C_h} \times \overline{Q_h} \times 24 \tag{1}$$

where $\overline{C_h}$ is the daily average of hourly NO_x concentration, mg m^{-3}; $\overline{Q_h}$ is the daily average of hourly wet flue gas flow under actual working condition, m^3 h^{-1}, and 24 is convert hour to day. Following the "Specifications and test procedures for a continuous emission monitoring system for SO_2, NO_x, and particulate matter in flue gas emitted from stationary sources (HJ/T76-2017)", the uncertainty of NO_x concentration (C_h) is less than or equal to 30% for the data used in this study. After quality control, the emission intensity on a grid-by-grid basis is found to be 0.64±0.08 μg m^{-2} s^{-1}, 0.45±0.13 μg m^{-2} s^{-1}, and 0.41±0.05 μg m^{-2} s^{-1} for 2019, 2020 and 2021, respectively. Probability density functions (PDFs) of daily emission intensity and a map of the multi-year mean are displayed in Fig. 3. The proportion of low values is highest in 2020, which is closely related to the epidemic in 2020, during which many key enterprises spontaneously shutting down or otherwise limited production. The highest emission intensity is observed in 2019, consistent with the decade-long decrease in emissions in China.

Table 1: Summary statistics for plants included in CEMS.

Year	Number of companies	Number of sacks monitored	Number of days without public data	Percentage of days without public data (%)
2019	624	1607	102	27.9
2020	705	1819	24	6.6
2021	714	1836	0	0

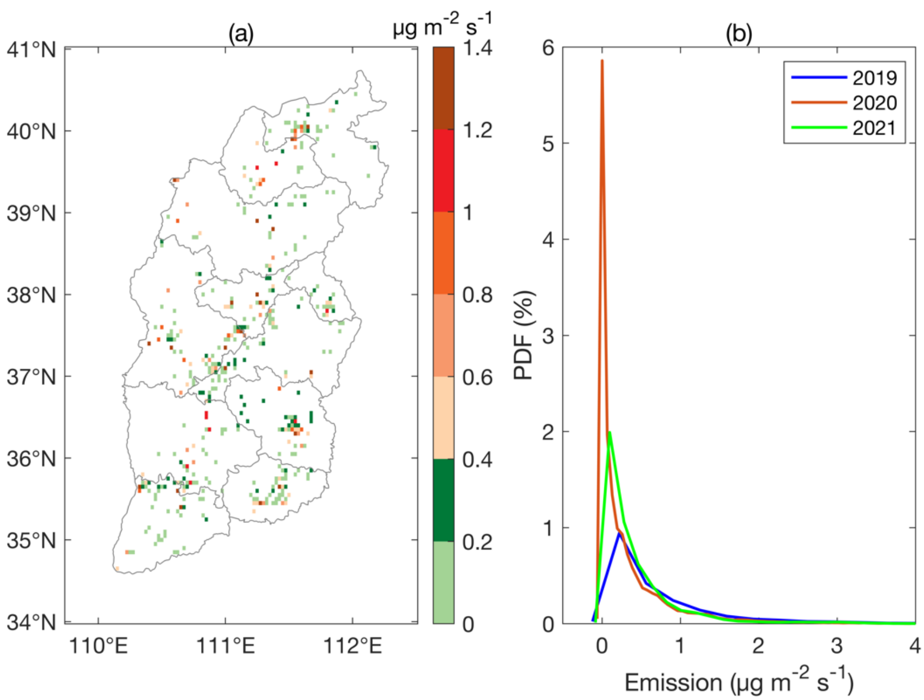

https://doi.org/10.5194/egusphere-2023-2
Preprint. Discussion started: 9 February 2023

Figure 3: CEMS emissions intensity from January 2019 through December 2021 (unit: μg m^{-2} s^{-1}): (a) 3-year average gridded NO_x emissions, and (b) PDFs of day-by-day and grid-by-grid emissions over individual years.

2.2.2 MEIC

MEIC provides bottom-up emissions of anthropogenic air pollutants over mainland China, with a monthly time step and a 0.25°×0.25° spatial resolution. NO_x is provided over five sectors: agriculture, industry, power, residential and transportation. This work uses data from 2019 and 2020 (Zheng et al., 2021). To match with the higher resolution TROPOMI grids, all of the MEIC data in this work is mapped uniformity to a 0.05 °×0.05 ° grid, with each TROPOMI sized grid assigned the same flux as the underlying MEIC grid. The average emission values and PDFs of the grid-by-grid data over Shanxi from 2019 January to 2020 December are given in Fig. 4(a) and (b).

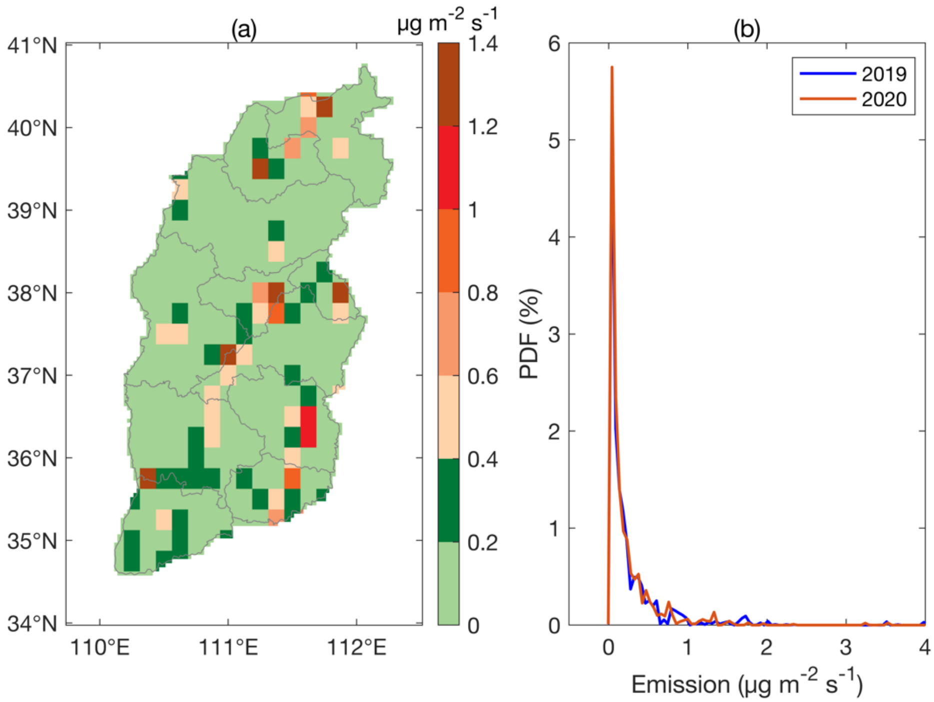

Figure 4: MEIC emissions intensity from January 2019 through December 2020 (unit: μg m^{-2} s^{-1}): (a) 2-year average monthly MEIC emissions, and (b) PDFs of month-by-month and the grid-by-grid emission over individual years.

2.3 Wind

Wind speed and direction are from the European Centre for Medium-Range Weather Forecasts, ERA-5 reanalysis product. This work uses the hourly 6:00 UTC u and v wind products (closest in terms of time to the TROPOMI overpass) at 850 hPa and 0.25 °×0.25 ° resolution, available at https://www.ecmwf.int/en/forecasts/dataset/ecmwf-reanalysis-v5. The wind was linearly interpolated to follow the TROPOMI 0.05 °×0.05 ° grid data in space and time. The reason for choosing the 850 hPa (which is approximately 1500 m) level is two-fold. First, Shanxi has complex topography, with less than 16% of the total area of the province under 800 m in height, 68% of the surface over 1000 m, and 17% of area over 1500 m, see Fig. 1, leading to a significant amount of pollutant transport from near the ground to the lower free troposphere. Second, due to the relatively dry conditions, vertical plume-based rise is thought to not be insignificant (Wang et al., 2020). Overall, we aim to use wind speed and direction that correspond to a reasonable approximation of the median of the NO_x emissions vertical profile.

2.4 Variance Maximization

To extract the spatial and temporal features of the extremes of the remotely sensed NO_2 fields in an unbiased manner, the Empirical Orthogonal Functions Principal Components Analysis (EOF) is applied. This technique decomposes the data into a set of orthogonal standing signals in space [EOF] and in time [PC], with those signals contributing the most to the overall variance of the underlying dataset being selected, representing unique phenomenon that control the overall characteristics of the NO_2 columns (Zhou et al., 2016; Lin et al., 2020). Further details including mathematical derivations are given in (Björnsson and Venegas, 1997) and (Cohen, 2014). This work retains the first three EOFs, which are found to contribute to 29.4%, 8.4%, and 4.4% of the total variation, with subsequent EOFs each contributing an insignificant amount (less than 4.0%) and therefore no longer considered in this work.

2.5 Model Free Inversion Estimation Framework

The Model Free Inversion Estimation Framework (MFIEF) is based on a mass balance assumption Eq. (2), and the detail is shown in Fig. 5 and Eq. (3). In the case where there is an observed change in the stock of NO_x in the atmosphere, herein represented as C, in a Lagrangian sense, there must be either a source or sink (Harte, 1988; Seinfeld and Pandis, 1997). When dealing with a fixed spatial grid, such as in this work, there is also a contribution from transport to or from the Lagrangian parcel. The first of these changes in the stock is due to the amount of NO_x emitted, herein represented as E, which always will increase the existing stock. The second of these is the chemical loss of NO_x, which will always lead to a decrease in the stock. The chemical sink of NO_x is dominated by the reaction between NO_2 and OH (Beirle et al., 2019; Valin et al., 2013), which herein is described as S. The third change in the stock is the sum of pressure induced and advective transport, which may either increase or decrease the stock. The transport is herein is described as D, and is calculated by the gradient of the product of the wind vector and the NO_x column loading, which consists of an advective portion (Wang et al., 2014) and a pressure-based portion (Mahowald et al., 2005). The mass conservation equation for NO_x is then calculated as

$$dC = E - S + D \tag{2}$$

Solving Eq. (2) for emissions on a grid-by-grid basis requires knowledge of the mass change of the loading in time and space, and detailed consideration of chemical loss and transformation, and transport. An explicit formulation of these processes into a readily solvable mass balance method is derived as Eq. (3):

$$E_{NOx} = \alpha_1 \cdot \frac{dV_{NO_2}}{dt} + 24 \cdot \frac{\alpha_1}{\alpha_2} \cdot V_{NO_2} + 0.001 \cdot \frac{\alpha_1}{\alpha_3} \cdot (\nabla(\boldsymbol{u} \cdot V_{NO_2}) + \nabla(\boldsymbol{v} \cdot V_{NO_2})) \tag{3}$$

https://doi.org/10.5194/egusphere-2023-2
Preprint. Discussion started: 9 February 2023

Where E_{NOx} represents the total atmospheric column emissions of NO_x within the troposphere on a grid-by-grid and time-by-time basis., with a unit of μg m^{-2} day^{-1}. This is the total emission into each column accounting for all sources including anthropogenic sources (industry, vehicle, and residential), biomass burning, and others. V_{NO2} represents the tropospheric NO_2 column concentration after it has been converted into the unit of μg m^{-2}. Due to the fact that TROPOMI only measures NO_2 and not NO_x, a transformation is required to transform NO_2 columns into NO_x, hereafter given as $NO_x = \alpha_1 \cdot NO_2$. $\alpha_1 \cdot \frac{dV_{NO_2}}{dt}$ computes the NO_x concentration change rate with a unit of μg m^{-2} day^{-1}, assuming the day-to-day temporal derivative of NO_2 exists in the TROPOMI data on the respective days. $24 \cdot \frac{\alpha_1}{\alpha_2} \cdot V_{NO_2}$ represents as the sink of NO_x concentration, where α_2 is related to the NO_x lifetime (unit h), and 24 is the unit change factor. $\nabla(\boldsymbol{u} \cdot V_{NO_2}) + \nabla(\boldsymbol{v} \cdot V_{NO_2})$ represents the divergence of NO_2 grid-by-grid with a unit of μg m^{-2} day^{-1}, assuming the grid-to-grid spatial gradient of TROPOMI NO_2 and reanalysis wind both exist on the respective grids. Maps of daily zonal and meridional fluxes were derived by multiplying gridded V_{NO2} with spatially gridded wind vector (Cohen and Prinn, 2011). In this case, α_3 is the parameter representing the transport distance (km) per day, where 0.001 is convert m to km. In all cases, the values of α_1 α_2 and α_3 are computed month-to-month and grid-by-grid based on the best fits of all individual daily data within each individual grid, or by the bootstrap method on a grid-to-grid and month-by-month basis.

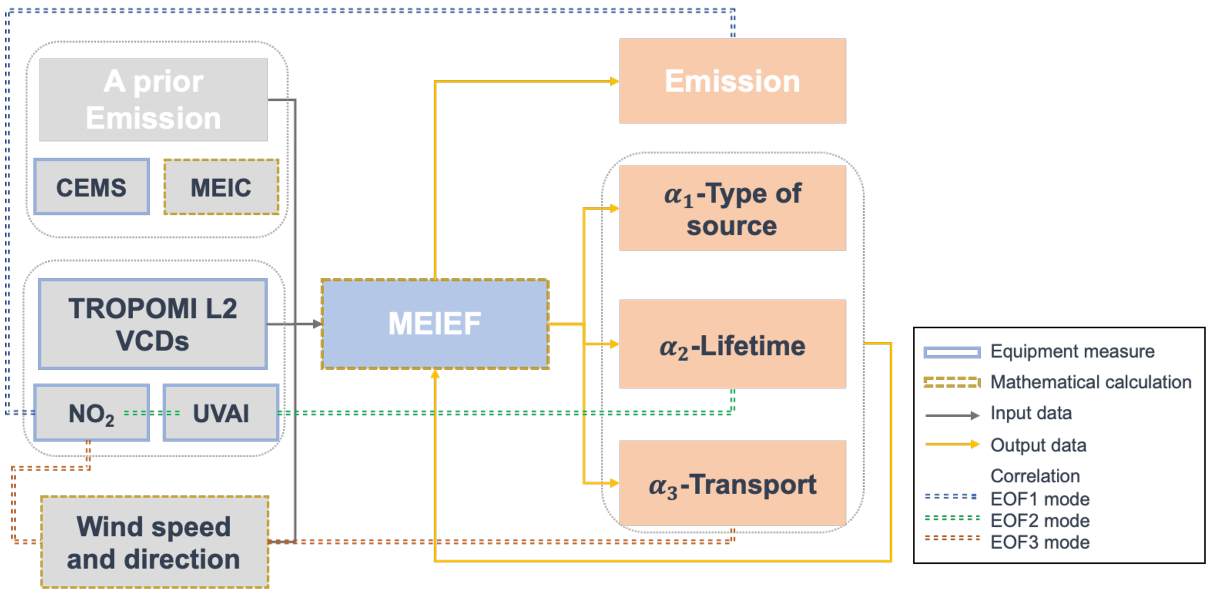

Figure 5: The framework of MEIEF methodology.

2.6 Additional Analytical Methods

This work employs multiple linear regression to fit the values of α_1, α_2, and α_3 on a month-by-month, grid-by-grid basis using all available daily measurements and Eq. (3). The values of α_1, α_2, and α_3 are further filtered based on both statistics ($p<0.15$,

https://doi.org/10.5194/egusphere-2023-2
Preprint. Discussion started: 9 February 2023

and removal of outliers defined as elements more than three scaled MAD from the median, calculated by Eq. (4)) and being physically realistic ($|\alpha_1|>1$, $\alpha_2<0$).

$$MAD = c \times median(abs(\alpha - median(\alpha))) \tag{4}$$

$$c = \frac{-1}{\sqrt{2} * erfcinv(\frac{3}{2})} \approx 1.483$$

α_1, α_2, and α_3 are brought into α in Eq. (4) respectively for outlier rejection. Bootstrapping is used as a means to create a new sample to represent the parent sample distribution through multiple repetitions of sampling (Liu and Cohen, 2022). Specifically, the distributions of α_1, α_2, and α_3 are sampled across the central 80% of their probability distributions, which are then used to generate a set of pseudos α_1, α_2, and α_3 on a grid-by-grid basis where there is no existing a priori and therefore no actual solution of these variables. These bootstrapped pseudo α_1, α_2, and α_3 are then used on these specific grids to approximate the emissions of NO_x using Eq. (3) on a daily basis where TROPOMI NO_2 column data and wind data is available. the mean data has been taken out as the daily results. The standard deviation of each grid was calculated as the uncertainty of this emission.

3 Results and Discussion

3.1 Computed Emissions Using CEMS and MEIC

The daily emissions of NO_x are calculated throughout the given spatial and temporal domain using bootstrapping in connection with Eq. (3) and the fitted values of α_1, α_2, and α_3. Figures 6(a) and (b) show the spatial distribution of daily average and variation of NO_x emissions based on CEMS (EI_{CEMS}) from Jan 2019 to Dec 2021 over Shanxi at 0.05° × 0.05°. For all subsequent emissions values displayed, the numbers correspond to the sum over the day-to-day mean ± uncertainty. It is observed that the grids with the highest NO_x emission in Shanxi are mainly concentrated in the lower Fen River valley, which happens to also be located at the lowest altitude areas in the province as shown in Fig. 1 pink line area. containing Taiyuan Basin, Xinding Basin, and LinFen Basin, which also corresponds to the area containing the highest population density. This area in total accounts for around 25% of the total area of the province and contributes 52% (0.96±0.55 Tg per year) of the total NO_x emission (1.83±1.06 Tg per year) in Shanxi. It is of significance to note that regions with a moderate average density of emissions, ranging from 0.3 to 0.7 μg m^{-2} s^{-1}, contribute 61% (1.11±0.64 Tg per year) of the total emissions. The use of MFIEF can effectively optimize the distribution of the inventory and perform inventory correction based on satellite data, while complementing many areas where there is no existing emissions data, incomplete data, mis-characterized data, or data which may be reasonable on average but not account for daily-scale variability.

https://doi.org/10.5194/egusphere-2023-2
Preprint. Discussion started: 9 February 2023

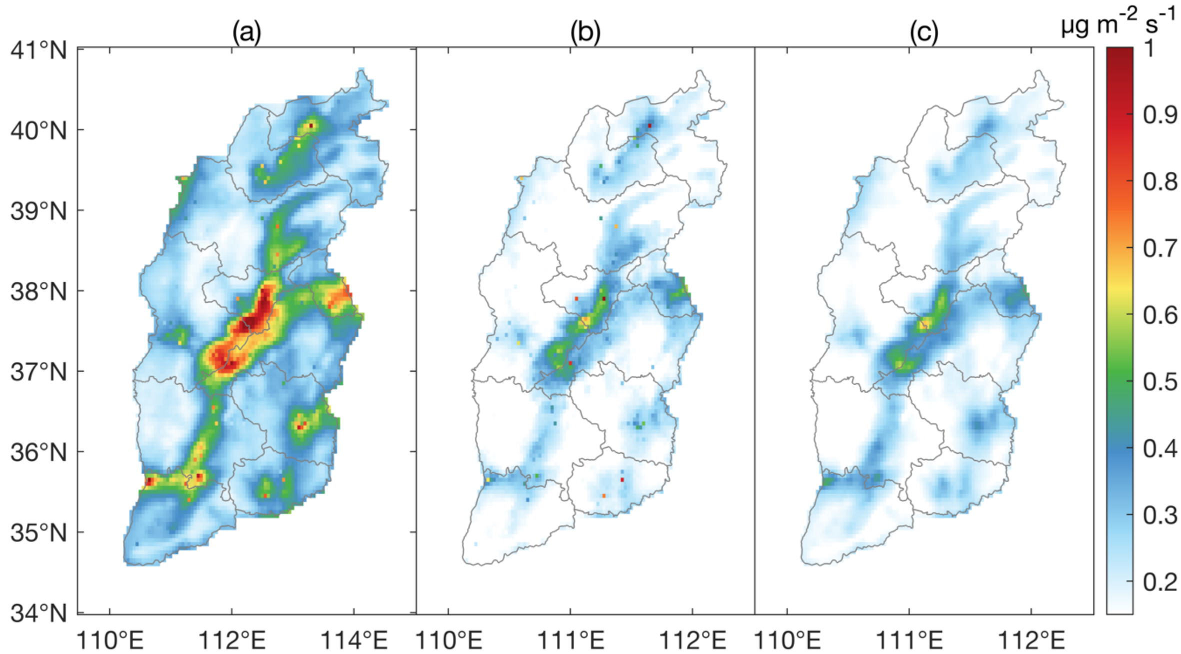

Figure 6: Daily average emissions based on CEMS from Jan 2019 to Dec 2021 over Shanxi at 0.05° × 0.05° (unit: μg m^{-2} s^{-1}): (a) daily average NO_x emissions. (b) day-to-day variability of NO_x emissions. (c) bootstrapping uncertainty range (10% to 90% of distribution).

MEIC was also separately used as the a priori with MFIEF to produce an additional emissions inventory from Jan 2019 to Dec 2020, herein called EI_{MEIC}. The total EI_{MEIC} over the province is 1.33±0.60 Tg per year. The multi-annual mean value of EI_{CEMS} minus EI_{MEIC} and the day-to-day and grid-to-grid emissions of both EI_{CEMS} and EI_{MEIC} from Jan 2019 to Dec 2020 are displayed in Fig. 7. On a multi-annual average basis, EI_{CEMS} is larger than EI_{MEIC} at 98% of grids, while on a day-to-day basis it is larger at 88% of grids. Some higher value appeared in EI_{MEIC} calculated by high MEIC values in some places of Shuozhou, Yangquan, Lvliang, Changzhi, and Jincheng may be due to mis-positioned hotspots in the existing inventories, in terms of both space and time. But on the opposite, EI_{CEMS} better captured in residential and small industrial sources than EI_{MEIC}.

This is possibly due to the fact that the a priori MEIC distribution has many low values which actually fall within the uncertainty of the bottom-up emissions processes (Cohen and Wang, 2014; Bond, 2004; Crippa et al., 2018). The low a priori emissions on a grid-by-grid basis, which in turn shift the physically filtered values of α_1 towards lower values. At the same time the values of α_2 were shifted to higher values. In tandem with these, the transport term α_3 was shifted to include larger absolute values of distance. This net combination caused the final calculation to be biased smaller overall.

Figure 8 shows the differences between CEMS, EI_{CEMS}, EI_{MEIC} and MEIC, and the 30% error range for CEMS and the computed the 10^{th} to 90^{th} percentile error ranges for EI_{CEMS} and EI_{MEIC} as computed from January 2019 to December 2020 in all 11 cities in Shanxi. It shows that while generally CEMS is larger than EI_{CEMS}, that they are always found to be within the error ranges of each other, while EI_{MEIC} only overlaps with CEMS in 4 cities. Similarly, MEIC is always found to be the lowest,

https://doi.org/10.5194/egusphere-2023-2
Preprint. Discussion started: 9 February 2023

while EI_{MEIC} is found to be larger than MEIC and smaller than EI_{CEMS}. In specific EI_{CEMS} and EI_{MEIC} have error ranges which overlap in all cities, while MEIC overlaps with the EI_{MEIC} range in 8 cities.

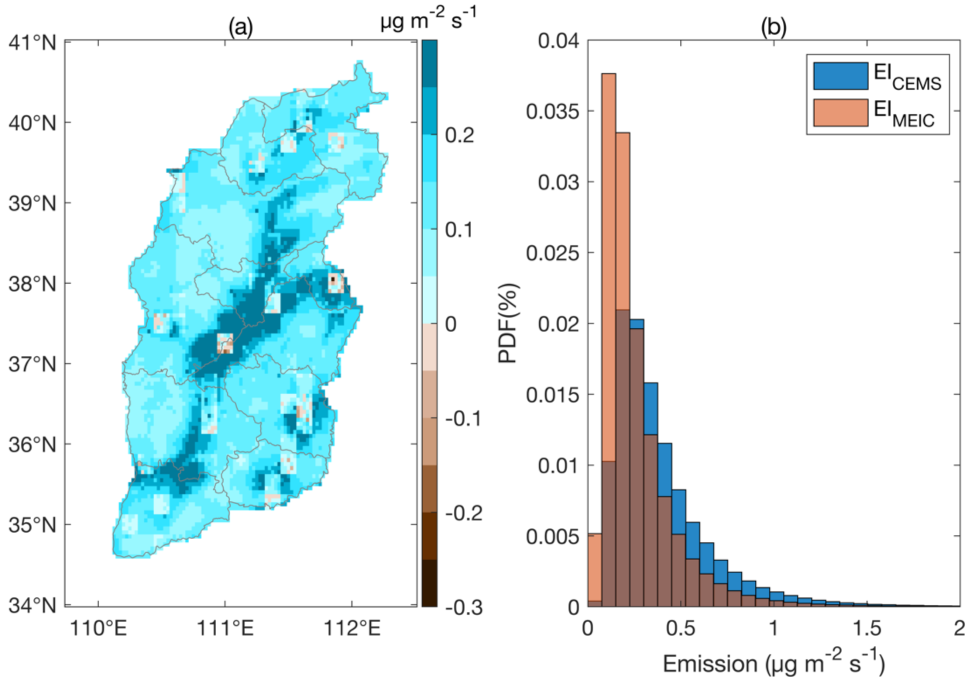

Figure 7: Differences between EI_{CEMS} and EI_{MEIC} through 2019 to 2020 (unit: µg m^{-2} s^{-1}): (a) average values in space of EI_{CEMS} minus EI_{MEIC}.
290 (b) Histogram of EI_{CEMS} and EI_{MEIC}.

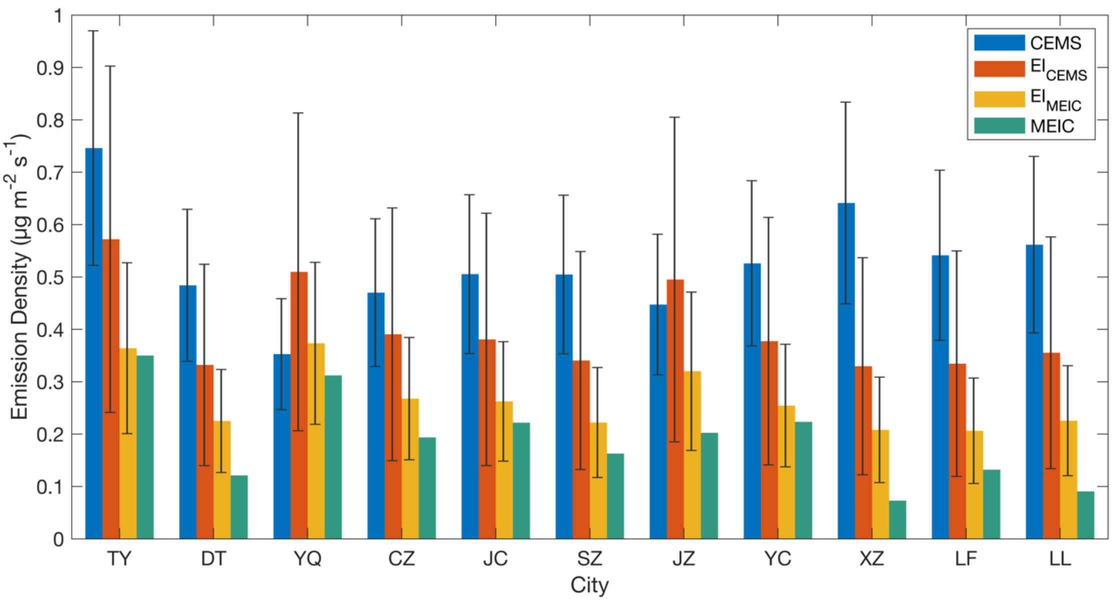

Figure 8: Differences between CEMS, MEIC, EI_{CEMS} and EI_{MEIC} with their error range through 2019 to 2020 in all 11 cities in Shanxi (unit: µg m^{-2} s^{-1}).

https://doi.org/10.5194/egusphere-2023-2
Preprint. Discussion started: 9 February 2023

3.2 Underlying Factors Contributing to Variance Maximized TROPOMI NO_2 Columns

A deeper analysis of the factors contributing to the variance in the TROPOMI NO_2 column measurements is essential to determine if the computed emissions and underlying factors are consistent with the remotely sensed fields both in terms of mean value and temporal variability. Recent practice has devised a way to ensure this consistency through the use of an EOF Analysis (Cohen et al., 2017; Cohen, 2014; Lin et al., 2020), which is applied to the daily TROPOMI NO_2 columns. The three spatial modes contributing the most variation to the observed daily TROPOMI NO_2 fields [EOF1, EOF2, and EOF3] contribute 29.4%, 8.4%, and 4.4% respectively, as shown in Fig. 9.

It is asserted that EOF1 is directly driven by EI_{CEMS}. The comparison of EOF1 and the emissions is shown in Fig. 10 in terms of both spatial and temporal scales. By applying four different progressively increasing cutoffs to the domain of EOF1, it is observed that as the EOF1 domain increases in magnitude, that the 3-year mean EI_{CEMS} computed over the same domains also increase in magnitude. Therefore, the more extreme the EOF1 value, the higher the emissions, demonstrating that the emissions are responsible for the first mode of the maximized variance. After detrending and removing any seasonal signal from EI_{CEMS}, the result correlates well with PC1 (r=0.66, p<0.01), indicating that the first mode of variation (PC1) is strongly connected with the changes in EI_{CEMS} in terms of both spatial and temporal dimensions.

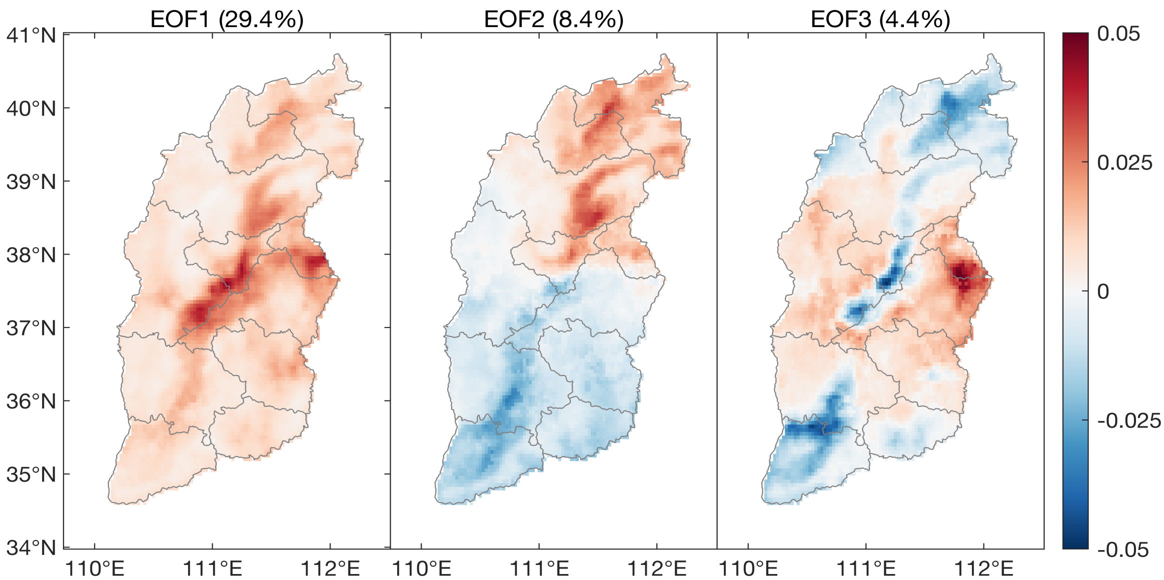

Figure 9: Spatial distribution map of first three modes (a) EOF1, (b) EOF2, and (c) EOF3.

https://doi.org/10.5194/egusphere-2023-2
Preprint. Discussion started: 9 February 2023

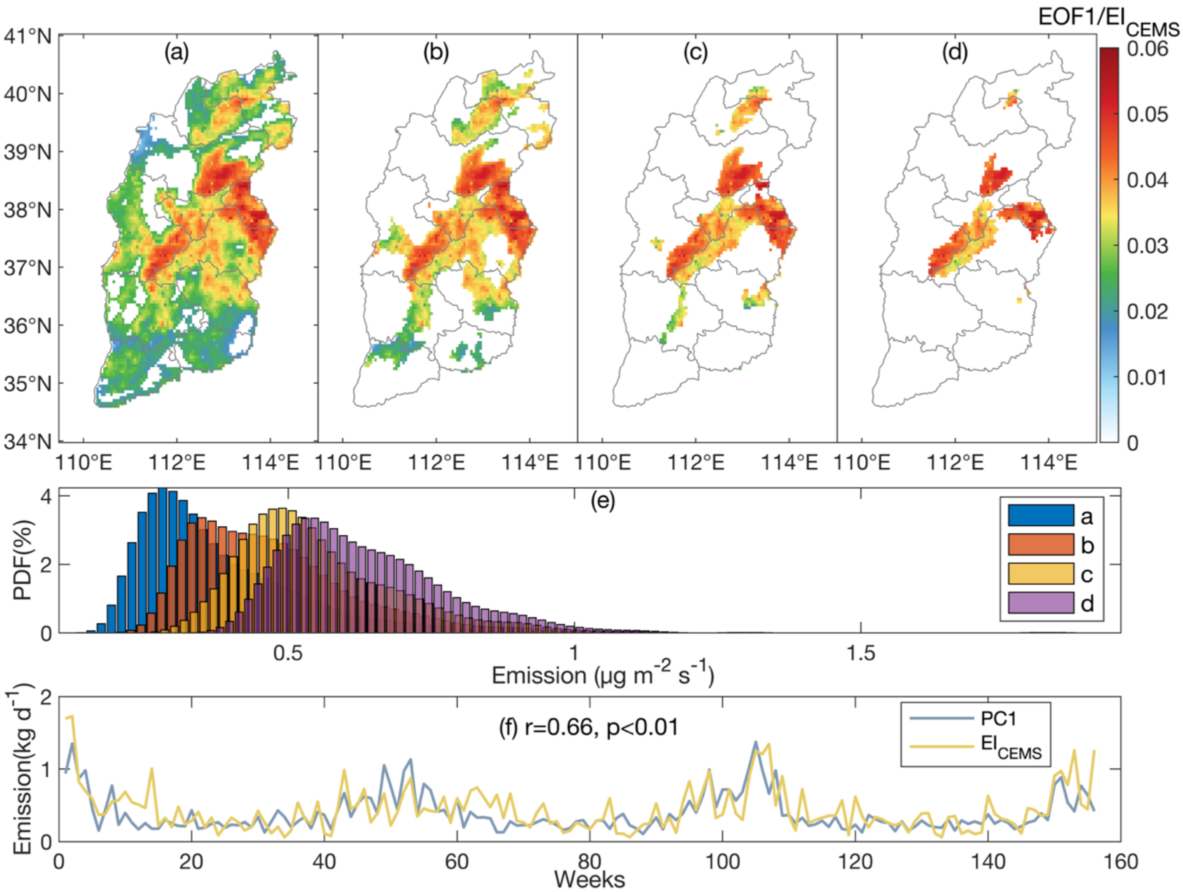

Figure 10: Four different cutoffs of EOF1 to set the domains. The maps in (a-d) are plots of EOF1/EI$_{CEMS}$ where the cutoffs are given as (a) EOF1 >0.005, (b) EOF1 >0.01, (c) EOF1 >0.015, (d) EOF1 >0.02. (e) Histograms of the EI$_{CEMS}$ over the domains given respectively in a-d. (f) Time series of weekly PC1 compare with EI$_{CEMS}$ in whole Shanxi.

Second, it is asserted that EOF2 is related to TROPOMI measured UVAI, which physically makes sense, since UVAI is a proxy of the absorbing aerosol loading, which itself directly constrains the UV in a cloud-free atmosphere. This change in UV radiation at the surface then changes the levels of OH, which then alter the chemical decay of NO_x. Applying four different cutoffs to EOF2, it is observed that as the EOF2 domain increase in magnitude, that the 3-year mean measured TROPOMI UVAI decreases, as demonstrated in Fig. 11. Since UVAI scales inversely with the available surface UV radiation, therefore lower UVAI implies higher available surface UV radiation, and implicitly faster chemical decay of NO_x, therefore demonstrating that the surface UV radiation is responsible for the second mode of the maximized variance. The negative correlation observed between absolute values of UVAI weighted by high absolute values of EOF2 grid-by-grid in the same EOF2 region is anticorrelated with PC2 (r=-0.35, p<0.01). While r in this case is a lot smaller, it is also consistent with theory, since in order to significantly affect the OH levels, the changes in UV radiation and hence UVAI must be very large, which is found to not occur frequently in time, but when it does occur, it makes a significant impact.

https://doi.org/10.5194/egusphere-2023-2
Preprint. Discussion started: 9 February 2023

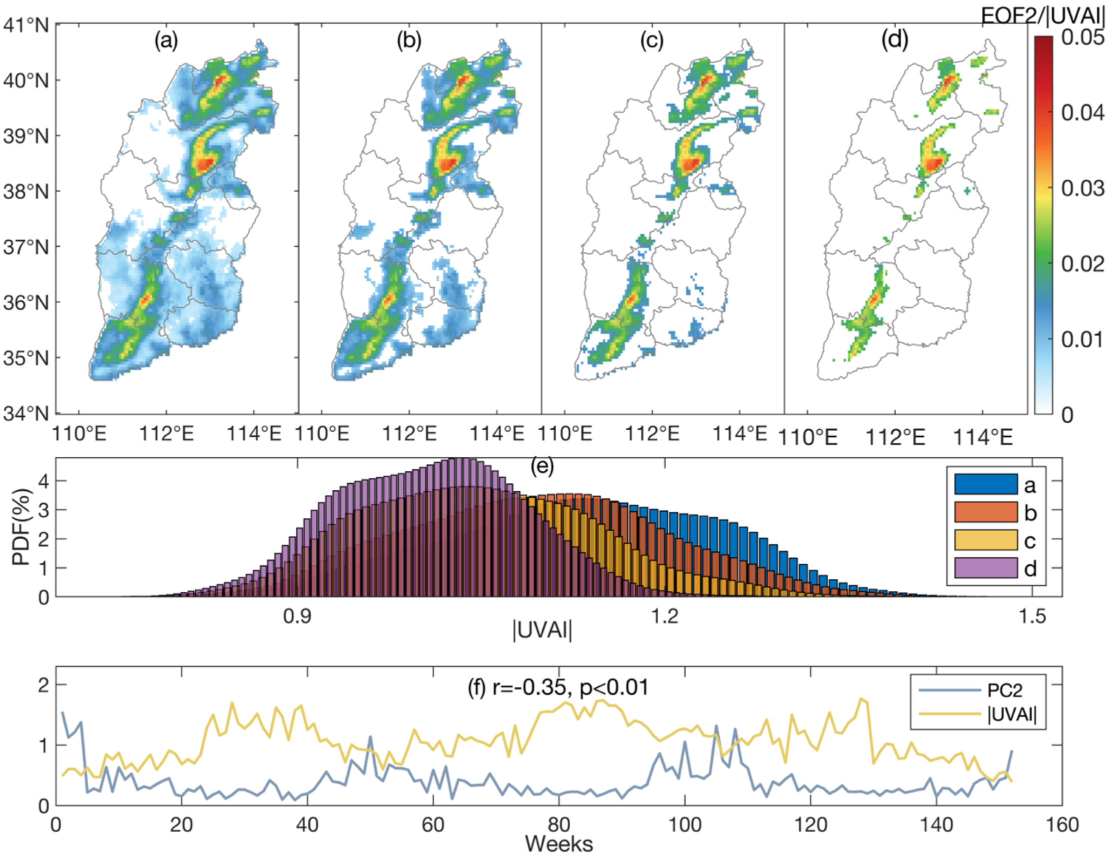

Figure 11: Four different cutoffs of EOF2 to set the domains. The maps in (a-d) are plots of EOF2/|UVAI| where the cutoffs are given as (a) EOF2 >0.005, (b) EOF2 >0.01, (c) EOF2 >0.015, (d) EOF2 >0.02. (e) Histograms of the UVAI over the domains given respectively in a-d. (f) Time series of weekly PC2 compare with |UVAI| in the (d) domain.

Finally, it is asserted that EOF3 is related to the transport of NO_2. This term has been specifically computed by taking the variance of the multiple of wind and TROPOMI measured NO_2 column loadings, specifically $\nabla(\boldsymbol{u} \cdot V_{NO2})$. Similarly, to the above cases, it is demonstrated that as four different cutoffs are applied to EOF3, it is observed that as the EOF3 domain increase in magnitude, so does the measured transport based on TROPOMI NO_2 also increase, as observed in Fig. 12. $\nabla(\boldsymbol{u} \cdot V_{NO2})$ weighted by EOF3 grid-by-grid positively correlates with PC3 (r=0.70, p<0.01), indicating that the third mode of variability, PC3 is strongly consistent with $\nabla(\boldsymbol{u} \cdot V_{NO2})$ in the temporal dimensions. Therefore, transport is responsible for the third mode of the maximized variance.

https://doi.org/10.5194/egusphere-2023-2
Preprint. Discussion started: 9 February 2023

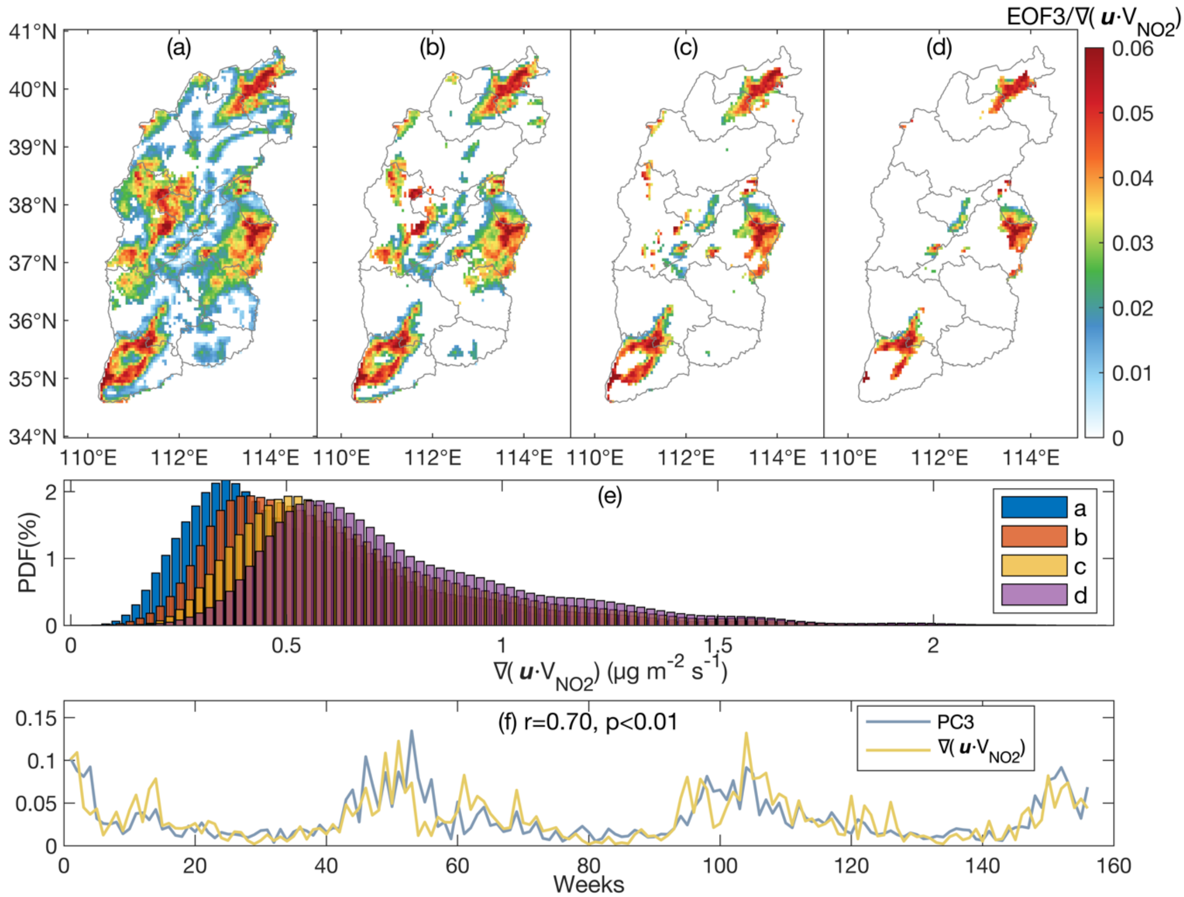

Figure 12: Four different cutoffs of EOF3 to set the domains. The maps in (a-d) are plots of EOF1/NO_2-transport where the cutoffs are given as (a) EOF3 >0.005, (b) EOF3 >0.01, (c) EOF3 >0.015, (d) EOF3 >0.02. (e) Histograms of the NO_2-transport over the domains given respectively in a-d. (f) Time series of weekly PC3 compare with $\nabla(\boldsymbol{u} \cdot \boldsymbol{V_{NO2}})$ in whole Shanxi.

3.3 Uncertainty in Emission and the parameters

The uncertainty of the computed emissions on a grid-by-grid and day-by-day basis is due to a combination of uncertainties in the satellite data, CEMS or MEIC a priori emissions, and the calculations involved with computing the various best-fit parameters. NO_x column concentrations and CEMS both have uncertainties about 30%. Another uncertainty comes from the parameters α_1, α_2, and α_3 generated during the regression of Eq. (3) as given in section 2.5. The fitted coefficients are computed month-by-month over the three years from January 2019 through December of 2021. Their absolute value overall mean, 10th percentile, and 90th percentile are found to be α_1=[4.0,1.3,8.3], α_2=[12.7,6.7,18.4] h, and α_3=[303,66,666] km. Due to the fact that the distributions are skewed to the lower end. However, it is observed in the fits that some amount of the variability is not uniform in space and time, with the month-by-month values and standard deviations given in Fig. 13. In general, α_1 tends to be slightly higher during the hotter months of the year, but it also has a higher variability when the UV values are high as well, making July and August the only months in which it statistically has fewer small values than the other times of the year. In

https://doi.org/10.5194/egusphere-2023-2
Preprint. Discussion started: 9 February 2023

general, α_2 tends to be variable, without any significant seasonal or month of year pattern. Instead, both inter-annual and intra-annual variations seem to drive most of the change. Given that this is related to both the column average temperature and UV availability, the largest values are found in June and the lowest values are found in April. Furthermore, there are other complex forcing factors including the height of the aerosol layer, the total aerosol loading, cloudiness, and other factors. The absolute magnitudes of α_2 and their uncertainty range are reasonable when compared with vertically integrated and 24-hour integrated chemical transport model values. In general, α_3 also seems to not have any significant seasonal or monthly pattern, with inter-annual and intra-annual terms seeming to dominate. The values tend to be slightly larger than chemical transport models account for, but are reasonable when compared with the ultra-long-range transport simulated for plumes which break the boundary layer. This range, combined with the wide basins of 200 km to 400 km in length, seem to provide a reasonable bound on the output results. One possible reason for this is that the atmospheric wind patterns were slightly different in 2019 due to the El Niño pattern (Hu et al., 2020). The result of overall uncertainty of the emissions as a result of the overall bootstrapped fitting ranges from 31% to 75% on a grid-by-grid basis, as shown in Fig. 3(c). In general, the larger relative uncertainty values are observed over mountain regions.

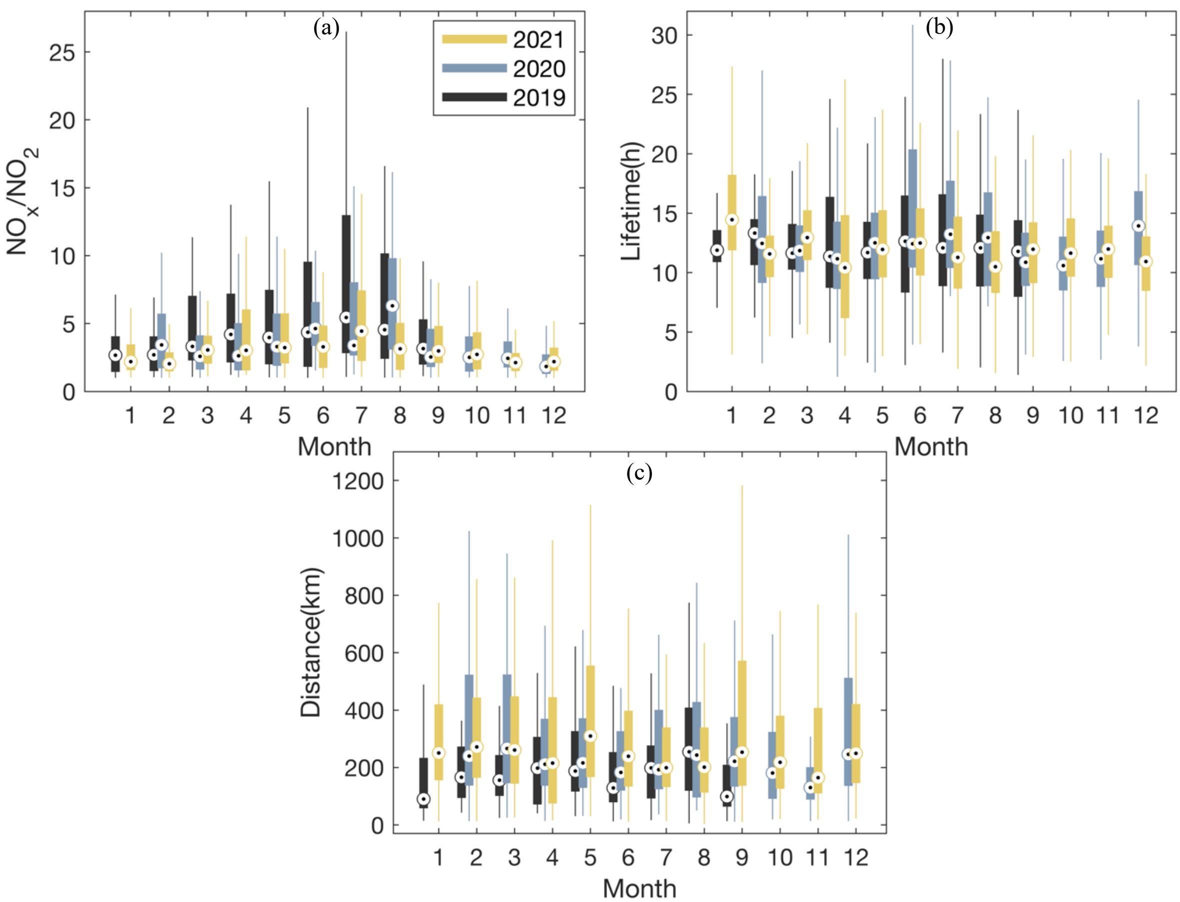

Figure 13: Distribution of monthly α_1 (a), α_2 (b) and α_3 (c) calculated based on CEMS.

https://doi.org/10.5194/egusphere-2023-2
Preprint. Discussion started: 9 February 2023

3.4 Application of α_1 to Analyze Different Combustion Technologies

A significant finding is observed when the value of α_1 is analyzed more closely on a pixel-by-pixel level and compared with underlying CEMS combustion source type. This analysis is motivated by the fact that NO_x is produced during high temperature combustion of air, with three different major parts contributing to the overall amount of NO_x produced: thermal NO_x formation, fuel NO_x formation and chemical NO_x formation (Schwerdt, 2006; Le Bris et al., 2007). This work demonstrates clearly that the values of α_1 are significantly related to the underlying thermodynamic conditions occurring at the time of combustion, allowing for many future applications of the results herein to better understand and monitor such plants around the world.

Thermal NO_x formation describes the process when N_2 in the air reacts with O_2 in the air at high temperatures (Le Bris et al., 2007), with NO_2 forming preferentially at temperatures between 800 °C and 1200 °C and NO forming preferentially at temperatures above 1200 °C. Thermal NO_x usually dominates the overall NO_x emissions when the temperature is over 1100 °C, and reaches a maximum contribution when the temperature is over 1600 °C. There is additional NO_x produced due to free nitrogen in the fuel itself. Finally, chemical decay may occur when there are mixed organo-nitrides, resulting in the prompt NO_x formation. Therefore, a deeper understanding of the overall and oxygen partial pressures and temperature in the combustion chamber are all important for NO_x formation. First, as the temperature increases, the amount of NO produced will increase along with NO_2. When the temperature exceeds 1200 °C, NO will continue to increase while NO_2 will decrease. Furthermore, when the pressure increases, the yield of NO_2 will also decrease and NO will increase (Aho et al., 1995; Turns, 1995).

In addition, in situ processes also impact the value of α_1 since there is a rapid adjustment after emitted from a combustion stack into the atmosphere, before the parcel comes to thermodynamic equilibrium (Cohen et al., 2018; Wang et al., 2020). From Fig. 12(a) it can be seen that the values are highest in the hottest months without maximum UV (July and August) and are lowest in the coldest months with the minimum UV (November, December, and January), with both factors moderating the combustion values during the atmospheric in situ processing time. This is especially important in the case of hotter power sources, since they will contain more buoyancy, and rise to a higher height, making them more likely to be in contact with air which is more exposed to UV and also generally colder than the surface. Overall, the value of α_1 seems to rely on both the temperature under which the initial NO_x was generated, as well as any rapid processes taking place once it is emitted into the atmosphere (including chemistry and vertical lofting).

A deeper look at the various different CEMS sources reveals that the internal combustion processes are extremely important in terms of the overall value of α_1. Production of cement is a major source of NO_x in Shanxi, with the major technology being dry process rotary kiln technology. Given that the temperature of the main burner of cement rotary kilns are higher than 1400 °C, with some peaking as high as 1800 °C to 2000 °C (Wu et al., 2020; Akgun, 2003), it is expected that there will be a large amount of thermodynamic NO_x generation. As observed at the cement CEMS sites, the computed α_1 has a value always within or above the error range of the values computed at powerplants, including some of the individually highest values, as show in Fig. 14(a).

Steel and iron are produced through a set of different processes, involving combustion at a range of different temperatures. The steps involved in the blast furnaces as well as some other processes, require a high flame temperature, in the range from 1350 ℃ to 2000 ℃. There are further processes occurring that require a relatively lower temperature, such as in the sinter bed stage, where the highest temperature is only about 1300 ℃ (Zhou et al., 2018). Therefore, while in general the values are relatively high, and are usually found within the ranges of power plants, there are some individual values of α_1 computed which are slightly outside the range of the power plant α_1 values, on both the high and low sides, as observed in Fig. 14(c). The maximum temperature of the combustion chamber of thermal power plants can reach 2000 ℃. In fact, such plants are constantly finding ways to increase the combustion efficiency, so that they can be more energy efficient and produce as much energy per ton of CO_2 emitted. As observed in Fig. 14(b), α_1 is relatively high at these sites, consistent with thermal production. Industrial boilers use a similar technology as power plants, but tend to be smaller and run at a lower temperature range and efficiency. This is because their use is to produce hot water and steam for direct residential and industrial use, not high-pressure steam to run turbines. In general, these boilers have a much smaller overall capacity (as small as one tenth of the total power output) and therefore without access to CEMS, may not be otherwise be detectable. However, analyzing the values of α_1 over these sites correspond to the CEMS map. For these reasons, it is logical that there is a greater amount of NO_2 produced than the above cases, and therefore as expected, the values of α_1 are significantly and consistently lower, as shown Fig. 14(e). Coke and aluminum oxide are both produced using a different technique from the other combustion sources, specifically focusing on creating high temperature, oven-like conditions to bake/roast their products. The average temperature of the coke oven charring chamber and aluminum oxide roasting furnace are around 1000 °C (Abyzov, 2019; Neto et al., 2021), with the material temperature continuously held in that temperature for a long period of time, e.g., one day. At the same time, the oxygen content is low. In net, there is far less thermal NO and more thermal NO_2. Aluminum is also smelted in an oven-like condition. Correspondingly, the values of α_1 are relatively lower, as detailed in Fig. 14(d) and Fig. 14(f).

https://doi.org/10.5194/egusphere-2023-2
Preprint. Discussion started: 9 February 2023

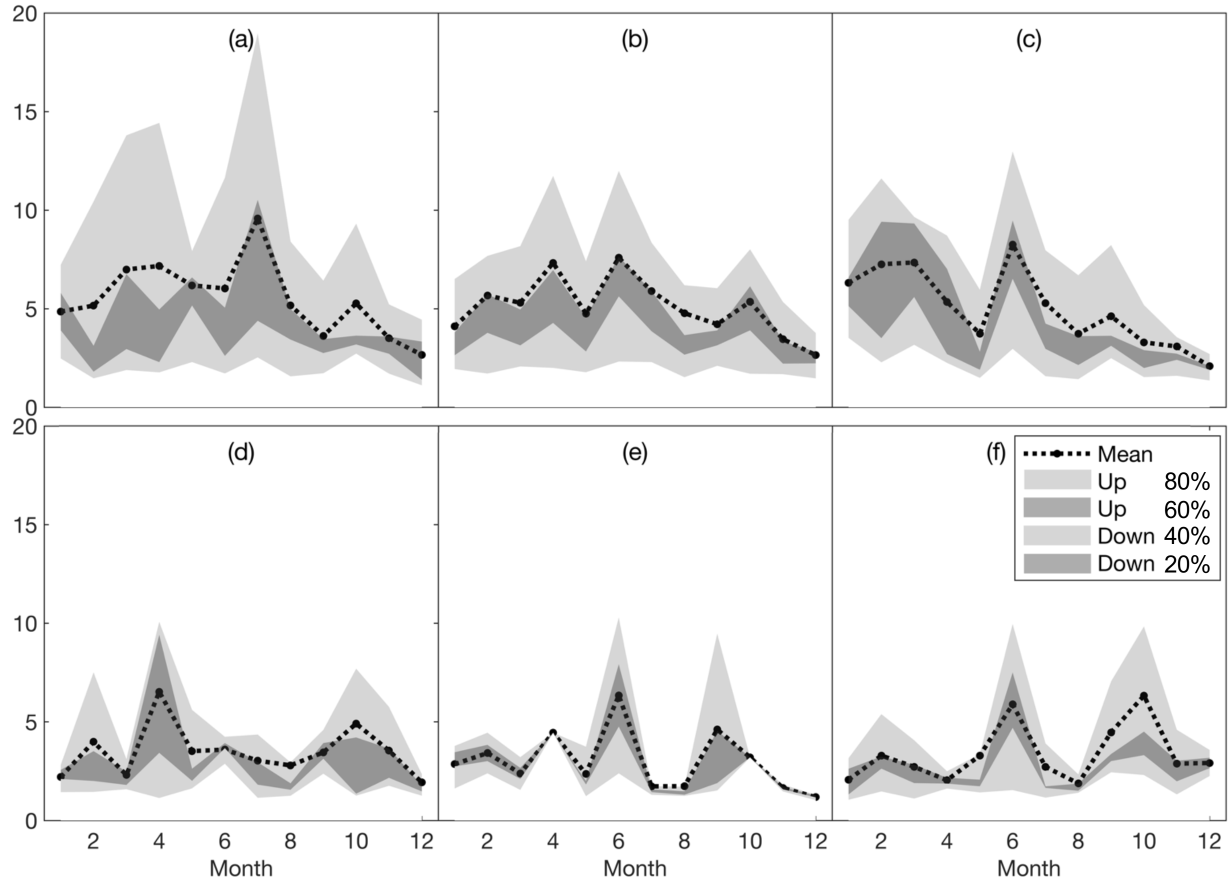

Figure 14: Distribution of monthly $\boldsymbol{\alpha_1}$ (mean values, 20th, 40th, 60th, and 80th percentile values) calculated based on CEMS using MFIEF at the following source: (a) cement factories; (b) power plants; (c) steel and iron factories; (d) coke ovens; (e) boilers; (f) aluminium oxide factories.

4 Conclusions

MFIEF based on daily measurements from TROPOMI and a priori daily emissions from CEMS successfully inverts daily NO_x emissions. First, the emissions computed matches well with known urban, suburban, and industrial locations. Secondly, the best fit values for thermodynamics (α_1) and first order chemical decay (α_2) are both physically realistic, while the best fit term for transport (α_3) is reasonable based on the mountain and basin geography of the province. Thirdly, the general variability in geography, month of the year, and years before and after COVID-19 are all consistent with what is known. Fourth, the uncertainty is observed to be lower than the day-to-day variability over 30% of the region, and mostly distributed in regions with higher emission intensities, showing that the results on a day-to-day basis are significant.

MFIEF emissions computed using different a priori datasets (CEMS versus MEIC) yield significant differences from on-the-ground CEMS measurements and local geospatial knowledge of where large sources exist. EI_{MEIC} severely underestimates

https://doi.org/10.5194/egusphere-2023-2
Preprint. Discussion started: 9 February 2023

sources which have a lower amount of emissions, as well as newer sources, while at the same time overestimates sources in Yangquan, Xiaoyi, and at the province's enormous steel and power plants, among other similar high emissions sources. EI_{MEIC} incorporates too many low values from MEIC in the suburban and rural areas, leading to many of these grids possessing physically unreasonable or at best very low/high values of α_1/α_2 values. A site-by-site comparison with CEMS shows very large differences with EI_{MEIC} at locations which MEIC do have an a priori value, indicating that any a priori dataset must be both precise and accurate, including on a day-to-day basis in order to present a good overall model fit and emissions output product. The MFIEF method as a procedure can quantitatively ally some of these shortcomings of present-day a priori inventories.

The results of variance maximization analysis of 3-years of daily TROPOMI NO_2 columns reveal 3 geospatial patterns that drive the variability in the NO_2 columns. EI_{CEMS} is attributed as responsible for pattern 1, measured UVAI from TROPOMI (which is inversely related to photochemistry) is attributed as responsible for pattern 2, while transport (computed from the gradient of reanalysis wind and TROPOMI NO_2 columns) is attributed as responsible for pattern 3. This procedure and its results form a basis of a best-practice approach that the community can adapt to subsequently analyze the efficacy of future emissions products. It is essential to ensure that emissions not only match on average, but also match well with the observed spatial and temporal gradients of the observed remotely sensed fields.

It is observed that the calculated values of α_1 are correlated with the thermodynamic conditions of underlying large combustion sources. This offers a new and self-consistent way to quantify the underlying combustion conditions of NO_x generation using remotely sensed measurements. At locations which have CEMS power plants α_1 is consistently high. At locations that have CEMS steel/iron and cement plants, α_1 is very high, but also has less consistency. Locations that have CEMS aluminum oxide plants, coke ovens, and boilers generally are low, but have a few individual high values of α_1. There is a slight offset based on the atmospheric temperature and UV radiation, with both colder and lower radiation months having α_1 slightly negatively offset and months with hotter temperature and higher radiation conditions having α_1 slightly positively offset. This is consistent across all plant types, but especially so for the hottest types (cement, iron/steel, and electricity), which are most likely to rise to a higher elevation and therefore be more impacted by the surrounding atmospheric conditions.

The procedure introduced here offers a next step advance in terms of computing emissions from a top-down perspective. Community adaptation and use of these new results will ideally allow improvement in bottom-up inventory constraints and attribution. This work would be improved by reduction in remotely sensed measurement errors/uncertainties, increased use of and access to surface CEMS and other high quality surface flux measurements, and improved a priori emissions databases. The adaptation of day-to-day and other higher frequency quantification data sources, especially sources with well quantified errors would also improve the work herein. The ability to identify large and moderately large plants and industrial sources could be used to identify and quantify sources from many parts of the Global South where ground-based measurements may not be readily available. It is hoped that the findings herein will be improved upon, possibly in an iterative manner, allowing for more precision and predictability, so that emissions and environmental regulators can have more quantitative support to focus their efforts.

Data Availability

The satellite NO_2 datasets used in this study are available at https://disc.gsfc.nasa.gov/datasets. The ERA-5 reanalysis product is available at https://doi.org/10.24381/cds.bd0915c6. The CEMS online data is available at https://sthjt.shanxi.gov.cn/wryjg. The MEIC product can be accessed from https://doi.org/10.6084/m9.figshare.c.5214920.v2. All of the data and underlying Figures are available for download at https://doi.org/10.6084/m9.figshare.20459889

Author Contributions

Xiaolu Li, Jason Blake Cohen, Kai Qin and Hong Geng developed the research question and set up the whole experimental program. Xiaolu Li wrote the manuscript and performed the data analysis with input from Jason Blake Cohen, Kai Qin, Rui Zhang, Liling Wu and Liqin Zhang. Liling Wu compared this result with the existing emission inventories and environmental statistics data. Liling Wu and Xiaohui Wu rectify the deviation of CEMS location and make statistics of annual changes. Jason Blake Cohen drafted and corrected the manuscript. Hong Geng, Xiaohui Wu, Chengli Yang, Rui Zhang, and Liqin Zhang supported consultation of the local situation and CEMS data. All authors discussed the results and contributed to the final manuscript.

Competing Interests

The authors declare that they have no conflict of interests.

Acknowledgments

The authors would like to thank the continuous emissions monitoring systems (CEMS) for the provision of their in situ data. This work thanks the PIs of the TROPOMI, ERA-5, MEIC products for making their data available. The study was supported by the National Natural Science Foundation of China (42075147), the Shanxi Province Major Science and Technique Program (202101090301013), and the Shanxi Province Postgraduate Education Innovation Program (2021Y035).

References

Abyzov, A.: Aluminum oxide and alumina ceramics (review). Part 1. Properties of Al_2O_3 and commercial production of dispersed Al_2O_3, Refract. Ind. Ceram., 60, 24-32, https://doi.org/10.1007/s11148-019-00304-2, 2019.

Aho, M. J., Paakkinen, K. M., Pirkonen, P. M., Kilpinen, P., and Hupa, M.: The effects of pressure, oxygen partial pressure, and temperature on the formation of N_2O, NO, and NO_2 from pulverized coal, Combust. Flame., 102, 387-400, https://doi.org/10.1016/0010-2180(95)00019-3, 1995.

https://doi.org/10.5194/egusphere-2023-2
Preprint. Discussion started: 9 February 2023

Akgun, F.: Investigaton of energy saving and NOx reduction possibilities in a rotary cement kiln, Int. J. Energ. Res., 27, 455-465, https://doi.org/10.1002/er.888, 2003.

Beirle, S., Boersma, K. F., Platt, U., Lawrence, M. G., and Wagner, T.: Megacity Emissions and Lifetimes of Nitrogen Oxides Probed from Space, Science, 333, 1737-1739, https://doi.org/10.1126/science.1207824, 2011.

Beirle, S., Borger, C., Dorner, S., Li, A., Hu, Z. K., Liu, F., Wang, Y., and Wagner, T.: Pinpointing nitrogen oxide emissions from space, Sci. Adv., 5, https://doi.org/10.1126/sciadv.aax9800, 2019.

Björnsson, H. and Venegas, S.: A manual for EOF and SVD analyses of climatic data, Open File Rep, Department of Atmospheric and Oceanic Sciences and Centre for Climate and Global Change Research, McGill University, 1997.

Bond, T. C.: A technology-based global inventory of black and organic carbon emissions from combustion, J. Geophys. Res, https://doi.org/109, 10.1029/2003jd003697, 2004.

Bond, T. C., Bhardwaj, E., Dong, R., Jogani, R., Jung, S., Roden, C., Streets, D. G., and Trautmann, N. M.: Historical emissions of black and organic carbon aerosol from energy-related combustion, 1850-2000, Global Biogeochem. Cycles, 21, GB2018, https://doi.org/10.1029/2006GB002840, 2007.

Cai, B., Liang, S., Zhou, J., Wang, J., Cao, L., Qu, S., Xu, M., and Yang, Z.: China high resolution emission database (CHRED) with point emission sources, gridded emission data, and supplementary socioeconomic data, Resour. Conserv. Recycl., 129, 232-239, https://doi.org/10.1016/j.resconrec.2017.10.036, 2018.

Chen, X., Liu, Q., Sheng, T., Li, F., Xu, Z., Han, D., Zhang, X., Huang, X., Fu, Q., and Cheng, J.: A high temporal-spatial emission inventory and updated emission factors for coal-fired power plants in Shanghai, China, Sci. Total. Environ., 688, 94-102, https://doi.org/10.1016/j.scitotenv.2019.06.201, 2019.

Chen, Y. H. and Prinn, R. G.: Estimation of atmospheric methane emissions between 1996 and 2001 using a three-dimensional global chemical transport model, Journal of Geophysical Research: Atmospheres, 111, https://doi.org/10.1029/2005JD006058, 2006.

Cohen, J. B.: Quantifying the occurrence and magnitude of the Southeast Asian fire climatology, Environ. Res. Lett., 9, https://doi.org/10.1088/1748-9326/9/11/114018, 2014.

Cohen, J. B. and Prinn, R. G.: Development of a fast, urban chemistry metamodel for inclusion in global models, Atmos. Chem. Phys., 11, https://doi.org/7629-7656, 10.5194/acp-11-7629-2011, 2011.

Cohen, J. B. and Wang, C.: Estimating global black carbon emissions using a top-down Kalman Filter approach, J. Geophys. Res. Atmos., 119, 307-323, https://doi.org/10.1002/2013jd019912, 2014.

Cohen, J. B., Lecoeur, E., and Hui Loong Ng, D.: Decadal-scale relationship between measurements of aerosols, land-use change, and fire over Southeast Asia, Atmos. Chem. Phys., 17, 721-743, https://doi.org/10.5194/acp-17-721-2017, 2017.

Cohen, J. B., Ng, D. H. L., Lim, A. W. L., and Chua, X. R.: Vertical distribution of aerosols over the Maritime Continent during El Nino, Atmos. Chem. Phys., 18, 7095-7108, https://doi.org/10.5194/acp-18-7095-2018, 2018.

Crippa, M., Guizzardi, D., Muntean, M., Schaaf, E., Dentener, F., van Aardenne, J. A., Monni, S., Doering, U., Olivier, J. G. J., Pagliari, V., and Janssens-Maenhout, G.: Gridded emissions of air pollutants for the period 1970–2012 within EDGAR v4.3.2, Earth Syst. Sci. Data, 10, 1987-2013, https://doi.org/10.5194/essd-10-1987-2018, 2018.

Geng, G., Xiao, Q., Zheng, Y., Tong, D., Zhang, Y., Zhang, X., Zhang, Q., He, K., and Liu, Y.: Impact of China's air pollution prevention and control action plan on $PM_{2.5}$ chemical composition over eastern China, Science China (Earth Sciences), 62, 1872-1884, https://doi.org/10.1007/s11430-018-9353-x, 2019.

Goldberg, D. L., Lu, Z., Streets, D. G., de Foy, B., Griffin, D., McLinden, C. A., Lamsal, L. N., Krotkov, N. A., and Eskes, H.: Enhanced Capabilities of TROPOMI NO_2: Estimating NO_x from North American Cities and Power Plants, Environ. Sci. Technol., 53, 12594-12601, https://doi.org/10.1021/acs.est.9b04488, 2019.

Green, A., Singhal, R., and Venkateswar, R.: Analytic extensions of the Gaussian plume model, J. Air Pollu. Control Assoc., 30, 773-776, https://doi.org/10.1080/00022470.1980.10465108, 1980.

Griffin, D., McLinden, C. A., Boersma, F., Bourassa, A., Dammers, E., Degenstein, D., Eskes, H., Fehr, L., Fioletov, V., Hayden, K., Kharol, S. K., Li, S. M., Makar, P., Martin, R. V., Mihele, C., Mittermeier, R. L., Krotkov, N., Sneep, M., Lamsal, L. N., Ter Linden, M., van Geffen, J., Veefkind, P., Wolde, M., and Zhao, X.: High resolution mapping of nitrogen dioxide with TROPOMI: First results and validation over the Canadian oil sands, Geophys. Res. Lett., 46, 1049-1060, https://doi.org/10.1029/2018GL081095, 2019.

Gu, X., Li, B., Sun, C., Liao, H., Zhao, Y., and Yang, Y.: An improved hourly-resolved NOx emission inventory for power plants based on continuous emission monitoring system (CEMS) database: A case in Jiangsu, China, J. Clean. Prod., 369, https://doi.org/10.1016/j.jclepro.2022.133176, 2022.

Harte, J.: Consider a spherical cow: A course in environmental problem solving, University Science Books, 1988.

Henk Eskes, J. v. G., Folkert Boersma, Kai-Uwe Eichmann, Arnoud Apituley, Mattia Pedergnana, Maarten Sneep, J. Pepijn Veefkind, and Diego Loyola: Sentinel-5 precursor/TROPOMI Level 2 Product User Manual Nitrogendioxide, Royal Netherlands Meteorological Institute Ministry of Infrastructure and Water Management, Open File Rep., 2021.

Hoesly, R. M., Smith, S. J., Feng, L., Klimont, Z., Janssens-Maenhout, G., Pitkanen, T., Seibert, J. J., Vu, L., Andres, R. J., Bolt, R. M., Bond, T. C., Dawidowski, L., Kholod, N., Kurokawa, J.-i., Li, M., Liu, L., Lu, Z., Moura, M. C. P., O'Rourke, P. R., and Zhang, Q.: Historical (1750–2014) anthropogenic emissions of reactive gases and aerosols from the Community Emissions Data System (CEDS), Geosci. Model Dev., 11, 369-408, https://doi.org/10.5194/gmd-11-369-2018, 2018.

Hu, P., Chen, W., Chen, S., Liu, Y., and Huang, R.: Extremely early summer monsoon onset in the South China Sea in 2019 following an El Niño event, Mon. Weather Rev., 148, 1877-1890, https://doi.org/10.1175/MWR-D-19-0317.1, 2020.

Jacob, D. J., Logan, J. A., Gardner, G. M., Yevich, R. M., Spivakovsky, C. M., Wofsy, S. C., Sillman, S., and Prather, M. J.: Factors regulating ozone over the United States and its export to the global atmosphere, J. Geophys. Res. Atmos., 98, 14817-14826, https://doi.org/10.1029/98JD01224, 1993.

https://doi.org/10.5194/egusphere-2023-2
Preprint. Discussion started: 9 February 2023

Jiang, X., Li, G., and Fu, W.: Government environmental governance, structural adjustment and air quality: A quasi-natural experiment based on the Three-year Action Plan to Win the Blue Sky Defense War, J. Environ. Manage., 277, 111470, https://doi.org/10.1016/j.jenvman.2020.111470, 2021.

Karplus, V. J., Zhang, S., and Almond, D.: Quantifying coal power plant responses to tighter SO_2 emissions standards in China, Proc. Natl. Acad. Sci. U S A, 115, 7004-7009, https://doi.org/10.1073/pnas.1800605115, 2018.

Kong, H., Lin, J., Zhang, R., Liu, M., Weng, H., Ni, R., Chen, L., Wang, J., Yan, Y., and Zhang, Q.: High-resolution (0.05° × 0.05°) NO_x emissions in the Yangtze River Delta inferred from OMI, Atmos. Chem. Phys., 19, 12835-12856, https://doi.org/10.5194/acp-19-12835-2019, 2019.

Lange, K., Richter, A., and Burrows, J. P.: Variability of nitrogen oxide emission fluxes and lifetimes estimated from Sentinel-5P TROPOMI observations, Atmos. Chem. Phys., 22, 2745-2767, https://doi.org/10.5194/acp-22-2745-2022, 2022.

Le Bris, T., Cadavid, F., Caillat, S., Pietrzyk, S., Blondin, J., and Baudoin, B.: Coal combustion modelling of large power plant, for NOx abatement, Fuel, 86, 2213-2220, https://doi.org/10.1016/j.fuel.2007.05.054, 2007.

Li, H., Zhang, J., Wen, B., Huang, S., Gao, S., Li, H., Zhao, Z., Zhang, Y., Fu, G., and Bai, J.: Spatial-temporal distribution and variation of NO_2 and its sources and chemical sinks in Shanxi province, China, Atmosphere, 13, 1096, https://doi.org/10.3390/atmos13071096, 2022.

Li, M., Liu, H., Geng, G., Hong, C., Liu, F., Song, Y., Tong, D., Zheng, B., Cui, H., Man, H., Zhang, Q., and He, K.: Anthropogenic emission inventories in China: a review, Natl. Sci. Rev., 4, 834-866, https://doi.org/10.1093/nsr/nwx150, 2017a.

Li, M., Zhang, Q., Kurokawa, J. I., Woo, J. H., He, K., Lu, Z., Ohara, T., Song, Y., Streets, D. G., Carmichael, G. R., Cheng, Y., Hong, C., Huo, H., Jiang, X., Kang, S., Liu, F., Su, H., and Zheng, B.: MIX: a mosaic Asian anthropogenic emission inventory under the international collaboration framework of the MICS-Asia and HTAP, Atmos. Chem. Phys., 17, 935-963, https://doi.org/10.5194/acp-17-935-2017, 2017b.

Lin, C., Cohen, J. B., Wang, S., and Lan, R.: Application of a combined standard deviation and mean based approach to MOPITT CO column data, and resulting improved representation of biomass burning and urban air pollution sources, Remote. Sens. Environ., 241, 111720, https://doi.org/10.1016/j.rse.2020.111720, 2020.

Liu, J. and Cohen, J.: Quantifying the Missing Half of Daily NO_x Emissions over South, Southeast and East Asia, nature portfolio [preprint], https://doi.org/10.21203/rs.3.rs-1613262/v1, 11 May, 2022.

Liu, M., van der A, R., van Weele, M., Eskes, H., Lu, X., Veefkind, P., de Laat, J., Kong, H., Wang, J., Sun, J., Ding, J., Zhao, Y., and Weng, H.: A New Divergence Method to Quantify Methane Emissions Using Observations of Sentinel-5P TROPOMI, Geophys. Res. Lett., 48, 10, https://doi.org/1029/2021gl094151, 2021.

Mahowald, N. M., Baker, A. R., Bergametti, G., Brooks, N., Duce, R. A., Jickells, T. D., Kubilay, N., Prospero, J. M., and Tegen, I.: Atmospheric global dust cycle and iron inputs to the ocean, Global Biogeochem. Cycles, 19, https://doi.org/10.1029/2004gb002402, 2005.

https://doi.org/10.5194/egusphere-2023-2
Preprint. Discussion started: 9 February 2023

Martin, R. V.: Global inventory of nitrogen oxide emissions constrained by space-based observations of NO_2 columns, J. Geophys. Res., 108, https://doi.org/10.1029/2003jd003453, 2003.

Mijling, B. and van der A, R. J.: Using daily satellite observations to estimate emissions of short-lived air pollutants on a mesoscopic scale, J. Geophys. Res. Atmos., 117, https://doi.org/10.1029/2012JD017817, 2012.

Neto, G. F., Leite, M., Marcelino, T., Carneiro, L., Brito, K., and Brito, R.: Optimizing the coke oven process by adjusting the temperature of the combustion chambers, Energy, 217, 119419, https://doi.org/10.1016/j.energy.2020.119419, 2021.

Ohara, T., Akimoto, H., Kurokawa, J.-i., Horii, N., Yamaji, K., Yan, X., and Hayasaka, T.: An Asian emission inventory of anthropogenic emission sources for the period 1980–2020, Atmos. Chem. Phys., 7, 4419-4444, https://doi.org/10.5194/acp-7-4419-2007, 2007.

Qin, K., Shi, J., He, Q., Deng, W., Wang, S., Liu, J., and Cohen, J. B.: New Model-Free Daily Inversion of NO_x Emissions using TROPOMI (MCMFE-NOx): Deducing a See-Saw of Halved Well Regulated Sources and Doubled New Sources, ESS Open Archive [preprint], https://doi.org/10.1002/essoar.10512010.1, July 26, 2022.

Qu, Z., Henze, D. K., Theys, N., Wang, J., and Wang, W.: Hybrid Mass Balance/4D-Var Joint Inversion of NO_x and SO_2 Emissions in East Asia, J. Geophys. Res. Atmos., 124, 8203-8224, https://doi.org/10.1029/2018JD030240, 2019.

Schreifels, J. J., Fu, Y. L., and Wilson, E. J.: Sulfur dioxide control in China: policy evolution during the 10th and 11th Five-year Plans and lessons for the future, Energ Policy, 48, 779-789, https://doi.org/10.1016/j.enpol.2012.06.015, 2012.

Schwerdt, C.: Modelling NO_x-formation in combustion processes, MSc Theses, 2006.

Seinfeld, J. and Pandis, S.: Atmospheric chemistry and physics, New York, 1997.

Singh, A. and Agrawal, M.: Acid rain and its ecological consequences, Journal of Environmental Biology, 29, 15, 2007.

S5P MPC VDAF Validation Web Article: Nitrogen Dioxide Column Data: https://mpc-vdaf.tropomi.eu/ProjectDir/reports//pdf/S5P-MPC-VDAF-WVA-L2_NO2_20180904.pdf, last access: 18 December 2022.

Shanxi Province Ecology and Environment Status Bulletin (2015, 2020): https://sthjt.shanxi.gov.cn/zwgk/hjgb/hjzkgb/index.shtml, last access: 14 December 2022.

Tang, L., Xue, X., Qu, J., Mi, Z., Bo, X., Chang, X., Wang, S., Li, S., Cui, W., and Dong, G.: Air pollution emissions from Chinese power plants based on the continuous emission monitoring systems network, Sci. Data, 7, 325, https://doi.org/10.1038/s41597-020-00665-1, 2020.

Tang, L., Qu, J. B., Mi, Z. F., Bo, X., Chang, X. Y., Anadon, L. D., Wang, S. Y., Xue, X. D., Li, S. B., Wang, X., and Zhao, X. H.: Substantial emission reductions from Chinese power plants after the introduction of ultra-low emissions standards, Nature Energy, 4, 929-938, https://doi.org/10.1038/s41560-019-0468-1, 2019.

Tu, Q., Schneider, M., Hase, F., Khosrawi, F., Ertl, B., Necki, J., Dubravica, D., Diekmann, C. J., Blumenstock, T., and Fang, D.: Quantifying CH_4 emissions in hard coal mines from TROPOMI and IASI observations using the wind-assigned anomaly method, Atmos. Chem. Phys., 22, 9747-9765, https://doi.org/10.5194/acp-22-9747-2022, 2022a.

Tu, Q., Hase, F., Schneider, M., García, O., Blumenstock, T., Borsdorff, T., Frey, M., Khosrawi, F., Lorente, A., Alberti, C., Bustos, J. J., Butz, A., Carreño, V., Cuevas, E., Curcoll, R., Diekmann, C. J., Dubravica, D., Ertl, B., Estruch, C., León-

Luis, S. F., Marrero, C., Morgui, J. A., Ramos, R., Scharun, C., Schneider, C., Sepúlveda, E., Toledano, C., and Torres, C.: Quantification of CH_4 emissions from waste disposal sites near the city of Madrid using ground- and space-based observations of COCCON, TROPOMI and IASI, Atmos. Chem. Phys., 22, 295-317, https://doi.org/10.5194/acp-22-295-2022, 2022b.

Turns, S. R.: Understanding NO_x formation in nonpremixed flames: Experiments and modeling, Progress in Energy and Combustion Science, 21, 361-385, https://doi.org/10.1016/0360-1285(94)00006-9, 1995.

Valin, L. C., Russell, A. R., and Cohen, R. C.: Variations of OH radical in an urban plume inferred from NO2 column measurements, Geophysical Research Letters, 40, 1856-1860, https://doi.org/10.1002/grl.50267, 2013.

Veefkind, J. P., Aben, I., McMullan, K., Förster, H., de Vries, J., Otter, G., Claas, J., Eskes, H. J., de Haan, J. F., Kleipool, Q., van Weele, M., Hasekamp, O., Hoogeveen, R., Landgraf, J., Snel, R., Tol, P., Ingmann, P., Voors, R., Kruizinga, B., Vink, R., Visser, H., and Levelt, P. F.: TROPOMI on the ESA Sentinel-5 Precursor: A GMES mission for global observations of the atmospheric composition for climate, air quality and ozone layer applications, Remote. Sens. Environ., 120, 70-83, https://doi.org/10.1016/j.rse.2011.09.027, 2012.

Wang, H., Rasch, P. J., Easter, R. C., Singh, B., Zhang, R., Ma, P. L., Qian, Y., Ghan, S. J., and Beagley, N.: Using an explicit emission tagging method in global modeling of source-receptor relationships for black carbon in the Arctic: Variations, sources, and transport pathways, Journal of Geophysical Research: Atmospheres, 119, https://doi.org/10.1002/2014jd022297, 2014.

Wang, S., Cohen, J. B., Lin, C. Y., and Deng, W. Z.: Constraining the relationships between aerosol height, aerosol optical depth and total column trace gas measurements using remote sensing and models, Atmos. Chem. Phys., 20, 15401-15426, https://doi.org/10.5194/acp-20-15401-2020, 2020.

Wang, S., Cohen, J. B., Deng, W., Qin, K., and Guo, J.: Using a new top-down constrained emissions inventory to attribute the previously unknown source of extreme aerosol loadings observed annually in the Monsoon Asia free troposphere, Earth's Future, 9, https://doi.org/10.1029/2021ef002167, 2021.

Wu, H., Cai, J., Ren, Q., Shi, C., Zhao, A., and Lyu, Q.: A thermal and chemical fuel pretreatment process for NO_x reduction from cement kiln, Fuel Process. Technol., 210, 106556, https://doi.org/10.1016/j.fuproc.2020.106556, 2020.

Zavala, M., Herndon, S. C., Slott, R. S., Dunlea, E. J., Marr, L. C., Shorter, J. H., Zahniser, M., Knighton, W. B., Rogers, T., and Kolb, C.: Characterization of on-road vehicle emissions in the Mexico City Metropolitan Area using a mobile laboratory in chase and fleet average measurement modes during the MCMA-2003 field campaign, Atmos. Chem. Phys., 6, 5129-5142, https://doi.org/10.5194/acp-6-5129-2006, 2006.

Zhang, X. and Schreifels, J.: Continuous emission monitoring systems at power plants in China: Improving SO_2 emission measurement, Energ. Policy., 39, 7432-7438, https://doi.org/10.1016/j.enpol.2011.09.011, 2011.

Zhang, Z., Zang, Z., Cheng, X., Lu, C., Huang, S., Hu, Y., Liang, Y., Jin, L., and Ye, L.: Development of three-dimensional variational data assimilation method of aerosol for the CMAQ model: an application for $PM_{2.5}$ and PM_{10} forecasts in the Sichuan Basin, Earth Space Sci. 8, e2020EA001614, https://doi.org/10.1029/2020EA001614, 2021.

Zheng, B., Zhang, Q., Geng, G., Chen, C., Shi, Q., Cui, M., Lei, Y., and He, K.: Changes in China's anthropogenic emissions and air quality during the COVID-19 pandemic in 2020, Earth Syst. Sci. Data, 13, 2895-2907, https://doi.org/10.5194/essd-13-2895-2021, 2021.

Zheng, B., Tong, D., Li, M., Liu, F., Hong, C., Geng, G., Li, H., Li, X., Peng, L., and Qi, J.: Trends in China's anthropogenic emissions since 2010 as the consequence of clean air actions, Atmos. Chem. Phys., 18, 14095-14111, https://doi.org/10.5194/acp-18-14095-2018, 2018.

Zhou, H., Ma, P., Cheng, M., Zhou, M., and Li, Y.: Effects of temperature and circulating flue gas components on combustion and NO_x emissions characteristics of four types quasi-particles in iron ore sintering process, ISIJ Int., 58, 1650-1658, https://doi.org/10.2355/isijinternational.ISIJINT-2018-185, 2018.

Zhou, S., Davy, P. K., Wang, X., Cohen, J. B., Liang, J., Huang, M., Fan, Q., Chen, W., Chang, M., Ancelet, T., and Trompetter, W. J.: High time-resolved elemental components in fine and coarse particles in the Pearl River Delta region of Southern China: Dynamic variations and effects of meteorology, Sci. Total Environ., 572, 634-648, https://doi.org/10.1016/j.scitotenv.2016.05.194, 2016.